Journal of Iberian Geology (2018) 44:513–537
https://doi.org/10.1007/s41513-018-0069-z

RESEARCH PAPER

Sedimentology and diagenetic evolution of the Neogene 'Intermediate Sandstone Unit' in the halite deposits of the Granada Basin (SE Spain): the turning point in the change from marine to continental sedimentation

Adrián López-Quirós[1] · Mickael Barbier[2] · José M. Martín[3] · Xavier Guichet[2]

Received: 1 October 2017 / Accepted: 1 June 2018 / Published online: 12 June 2018

Abstract
The Granada Basin is a small (50 × 50 km) Neogene intramontane basin located in the central part of the Betic Cordillera (Spain). In the latest Tortonian, the Granada Basin desiccated and a thick salt succession formed, encompassing three halite-bearing units: the 'Lower Halite Unit', the 'Intermediate Sandstone Unit' (ISU), and the 'Upper Halite Unit' (UHU). ISU deposits record the onset of marine to non-marine conditions in the Granada Basin. The main purpose of this paper is to study the environment of formation and the diagenetic evolution of the ISU salt-bearing unit, in order to assess the events leading to and resulting from the continentalization of this basin in the late Miocene. This study includes visual core descriptions, petrographic (conventional petrography and scanning electron microscopy), and geochemical ($\delta^{34}S$ and $\delta^{18}O$ and $^{87}Sr/^{86}Sr$) analyses. ISU deposition took place in a coastal lake, isolated from the open sea by a sand barrier. Lake evolution was from a very shallow, hypersaline lacustrine environment to a deeper, perennial lake undergoing frequent storm-induced marine flooding and, finally, to a shallower, perennial saline lake. Isotope analyses point to a mixture of different inflow waters, including marine- and underground (hydrothermal)-water inputs for the origin of the brines. Halite dissolution occurred after flooding events and clear-halite cement was precipitated inside primary-halite dissolution cavities. Early diagenesis involves halite re-crystallisation during repetitive, dissolution–precipitation cycles, gypsum replacement by halite, halite replacement by nodular anhydrite, and framboid pyrite formation. Intermediate- to late-diagenetic processes are silica (megaquartz, chalcedony, and lutecite) replacement of halite and anhydrite, and celestine replacement. Megaquartz formation relates to sulfate-depleted, UHU percolating brines. Chalcedony and lutecite crystallization took place sometime later from sulfate-rich percolating brines, during deposition of the gypsum sequence occurring on top of the salt. Celestine, replacing lutecite, resulted from the interaction with Sr-rich underground waters (via dissolution of previously formed celestine).

Keywords Granada Basin · Late Tortonian · Marine–continental transition · Evaporites · Diagenesis · Brine evolution

Resumen
La Cuenca de Granada (50 × 50 km) es una cuenca neógena intramontañosa ubicada en la parte central de la Cordillera Bética (España). Al final del Tortoniense se desecó, depositándose una potente secuencia salina, formada por tres unidades que incluyen halita: la 'Unidad de Halita Inferior' (UHI), la 'Unidad de Arenisca Intermedia' (UAI) y la 'Unidad de Halita Superior' (UHS). Los sedimentos de la UAI registran el cambio de condiciones marinas a no marinas. El objetivo principal de este trabajo es estudiar el ambiente de formación y la evolución diagenética de la UAI, para evaluar los eventos que condujeron y resultaron de la continentalización de esta cuenca en el Mioceno tardío. Este estudio incluye descripciones visuales de los testigos de sedimento, análisis petrográficos (petrografía convencional y Microscopía Electrónica de Barrido) y geoquímicos ($\delta^{34}S$, $\delta^{18}O$ y $^{87}Sr/^{86}Sr$). El depósito de la UAI tuvo lugar en un ambiente de lago costero, aislado del mar abierto por una isla barrera. El lago evolucionó de somero e hipersalino, a más profundo y con frecuentes inundaciones marinas inducidas por tormentas y, de nuevo a salino somero. Los análisis isotópicos indican mezcla de aguas, incluidas marinas y subterráneas (hidrotermales) para explicar el origen de las salmueras. Los eventos de inundación disolvieron parte de la

Extended author information available on the last page of the article

halita, reprecipitándola como cemento secundario en las cavidades de disolución. En la diagénesis temprana se produjo la recristalización de halita, el reemplazamiento de yeso por halita y el de halita por anhidrita nodular, y la formación de pirita framboidal. En la diagénesis intermedia-tardía tuvo lugar el reemplazamiento de halita y anhidrita por sílice (megacuarzo, calcedonia y lutecita), y el de la lutecita por celestina. La formación de megacuarzo se relaciona con salmueras de percolación empobrecidas en sulfato procedentes de la UHS. La cristalización de calcedonia y lutecita aconteció después a partir de salmueras de percolación ricas en sulfato, procedentes de la secuencia yesífera que corona la sal. El reemplazamiento de lutecita por celestina tuvo lugar por la interacción con aguas subterráneas ricas en Sr.

Palabras clave Cuenca de Granada · Tortoniense final · Transición marino-continental · Evaporitas · Diagénesis · Evolución de la salmuera

1 Introduction

Evaporites as a salt rock are originally made up of minerals that crystallized from brines saturated by solar evaporation (Sarg 2001; Trichet et al. 2001; Warren 2006, 2016). Large sequences of evaporites (saline crust and evaporite minerals) form in arid/semiarid climatic settings and restricted basins (Kendall and Harwood 1996; Schreiber and El Tabakh 2000; Warren 2010). In recent years, evaporites have been studied in relation to depositional environments (e.g. Taberner et al. 2000; Topper and Meijer 2013), mineralogy and geochemistry (e.g. Cendón et al. 2008; García-Veigas et al. 2013), tectonic setting (e.g. Ortí et al. 2014a), and sequence stratigraphy (e.g. Tucker 1991; Sarg 2001).

The study of evaporite units, based mainly on mineralogical and/or geochemical studies, is usually complemented by observations on the different sedimentological features of the salt deposit (Schreiber and El Tabakh 2000). When sediments still preserve their original mineralogy and morphologies, the precise paleo-environmental conditions can be inferred. Mineralogical studies in evaporite sequences provide information on the type of basin (i.e. marine vs. continental, e.g. Strakhov 1970), and the principal salt sources (solutes dissolved in seawater and recycling sources, e.g. Lotze 1957). However, for a better understanding concerning possible sources of original waters, geochemical analyses are also needed. The isotope composition of sulfates leads to the discerning of the marine vs. continental origin of the SO_2^{-4} ion (i.e. marine vs. continental by recycling of older evaporites, or by reoxidation of sulfides or elemental sulfur, e.g. Holser and Kaplan 1966; Nielsen 1972; Birnbaum and Coleman 1979). Chemical parameters during evaporite deposition as redox conditions can also be inferred from sulfate isotopes (e.g. Pierre 1985, 1989). $^{87}Sr/^{86}Sr$ isotope ratios have also been demonstrated to be a significant tool for documenting the marine vs. continental origin of evaporites. Studies linking mineralogical, petrological, sedimentological and geochemical analysis provide a full understanding of the depositional environment and paleohydrological evolution of evaporite basins (e.g. Lowenstein and Spencer 1990; Ayora et al. 1994a, 1995; Ortí et al. 2014a).

The Granada Basin, situated in the central part of the Betic Cordillera (SE Spain), contains a thick, uppermost Tortonian evaporite succession (the 'Lower Evaporites' of Dabrio et al. 1982), formed under transitional marine to continental conditions (Martín et al. 1984). This Evaporite Unit, from the margin to the center of the basin, has the following deposits: (a) gypsified stromatolites replaced by celestine (the 'Montevive and Escúzar Celestine' sensu Martín et al. 1984 and García-Veigas et al. 2015); (b) selenite gypsum (the 'Agrón Gypsum' sensu García-Veigas et al. 2015), and (c) halite (the 'Chimeneas Halite' sensu García-Veigas et al. 2013) (Fig. 1). In the salt succession (up to 500 m thick), García-Veigas et al. (2013) identified three halite-bearing units overlying a very thin, basal anhydrite bed: the 'Lower Halite Unit' (LHU), the 'Intermediate Sandstone Unit' (ISU) and the 'Upper Halite Unit' (UHU).

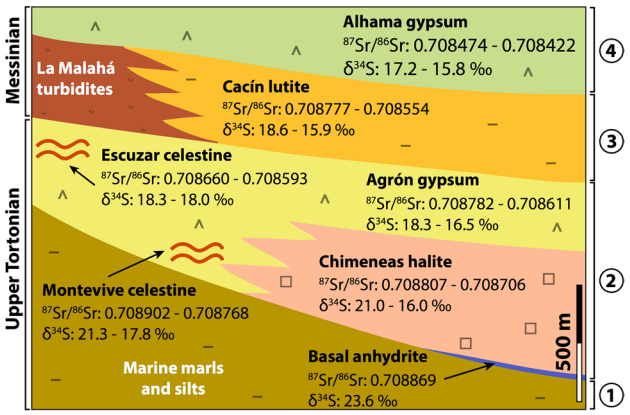

Fig. 1 Chemostratigraphic and lithostratigraphic correlation chart of the Upper Miocene evaporites and celestine ore-deposits in the Granada Basin (modified from García-Veigas et al. 2015). $^{87}Sr/^{86}Sr$ and $\delta^{34}S$ isotope data are from García-Veigas et al. (2013, 2015). The Lower Evaporites (Dabrio et al. 1982) comprise the Montevive and Escúzar Celestine, the Agrón Gypsum, and the Chimeneas Halite units (García-Veigas et al. 2015). The Alhama Gypsum (García-Veigas et al. 2015) corresponds to the Upper Evaporites (Dabrio et al. 1982). A clastic unit (Cacín Lutite and La Malahá Turbidites; Dabrio et al. 1982) occurs in between. (1) Open-marine sediments; (2) marine to continental, transitional deposits; (3–4) Lacustrine deposits

Previous works have concentrated on the study of the stromatolites and related celestine ore deposits (Martín et al. 1984; García-Veigas et al. 2015), on the gypsum (Dabrio et al. 1982; Dabrio and Martín 1981), and on the halite (García-Veigas et al. 2013), barely dealing with the intercalated 'clastic' sediments within the salt. This paper focuses on the study of these latter deposits, linking petrological, sedimentological, and isotope data to identify the environment of formation and the diagenetic evolution of this salt-bearing unit. As shown below, the ISU represents the first step in the growing influence of non-marine contributions to salt deposition in the Granada Basin, so it is an appropriate scenario for interpreting the events leading to and resulting from the continentalization of this basin in the late Miocene.

2 Geological setting

The Betic Cordillera (southern Spain) is the westernmost segment of the European Alpine Belt. Its paleogeographic and tectonic evolution relates to the closure of the Tethys Ocean in the Alpine Orogeny, during the Cenozoic (Savostin et al. 1986; Ziegler 1988; Dewey et al. 1989; Jabaloy et al. 2002). Differential uplifting during the Alpine Orogeny produced a number of sedimentary basins within the Betic Chain referred to as 'Neogene Basins'. Some of these basins opened directly to the Mediterranean Sea, while others maintained links with the Atlantic Ocean through the Guadalquivir foreland basin (Braga et al. 2003). The connections between the Mediterranean-linked basins and the Atlantic-linked basins were limited to a few seaways that progressively closed in the course of the late Miocene (Martín et al. 2014).

Two different types of Mediterranean-linked basins can be distinguished: the 'inner basins' (located far from the present-day Mediterranean Sea) and the 'outer basins' (near to the present-day Mediterranean Sea). The former group includes, from West to East, the Granada, Guadix-Baza, Fortuna and Lorca basins, while the latter group comprises the Tabernas, Almería-Níjar, Sorbas and Alicante-Bajo Segura basins (Braga et al. 2003) (Fig. 2a). These basins were progressively isolated from the Mediterranean Sea (from late Tortonian onward), until arriving at the present-day geographical situation (Sanz de Galdeano 1990; Sanz de Galdeano and Vera 1991, 1992; Braga et al. 2003; Sanz de Galdeano and Alfaro 2004; Krijgsman et al. 2006; Corbí et al. 2012). In the latest Tortonian–early Messinian, the inner basins were disconnected from the Mediterranean Sea and became continental, while the outer basins maintained their links, in some cases up to the Pliocene (Braga et al. 2003).

The Granada Basin is a small (50 × 50 km) Neogene intramontane basin located in the central part of the Betic Cordillera (Fig. 2). The basin's sedimentary infill unconformably overlies an irregular, fault-controlled, basement paleorelief (Morales et al. 1990), consisting of rocks from the two major domains of the Cordillera: the Internal Zones (cropping out at Sierra Tejeda, Sierra de la Pera, and Sierra Nevada) and the External Zones (cropping out at Sierra Gorda and Sierra Arana) (Fig. 2b). A series of sedimentary units can be differentiated in the Neogene–Quaternary infilling of the Granada basin (Martín et al. 1984; Braga et al. 1990, 2003) (Fig. 2b). Major fault systems have E–W orientations (Sanz de Galdeano 2008). Secondary faults, with a NW–SE trending, cut and displace the E–W faults and define the principal subsiding areas of the central and eastern part of the Granada Basin (Rodríguez-Fernández and Sanz de Galdeano 2006).

The Granada Basin as such differentiated in the late Tortonian (at around 8.3 Ma: Braga et al. 2003; Rodríguez-Fernández and Sanz de Galdeano 2006; Corbí et al. 2012). Initially, the basin was a marine embayment connected to the Atlantic Ocean to the northwest (Martín et al. 2014) and to the Mediterranean Sea to the south and west (Braga et al. 1990). From 8.3 to 7.3 Ma, major tectonic activity took place in the northeastern (Sierra Arana) and eastern (Sierra Nevada) highland edges of the basin (Fig. 2), resulting in the deposition of significant amounts of conglomerates at the base of the uplifted areas (Braga et al. 1990, 2003; Martín and Braga 1997). Skeletal carbonates accumulated in siliciclastic-free areas on platforms around the marine-basin margins. Temperate-water carbonates (Puga-Bernabéu et al. 2008; López-Quirós et al. 2016) formed first, between 8.3 and 7.8 Ma (Corbí et al. 2012), followed by tropical, coral-reef carbonates (Braga et al. 1990), between 7.8 and 7.3 Ma (Corbí et al. 2012). In the course of the late Tortonian, the marine connections to the Atlantic Ocean were interrupted first (Martín et al. 2014) and, finally, those to the Mediterranean Sea (Martín et al. 1984) due to a major regression resulting from a significant eustatic sea-level fall associated with local tectonic uplift. As a result the Granada Basin desiccated (Martín et al. 1984) and became continental in the latest Tortonian (7.3–7.2 Ma, Corbí et al. 2012).

During the Messinian and the Pliocene, the continental Granada Basin was filled by detrital (alluvial-fan and fluvial) and carbonate/evaporite (lacustrine) deposits (Dabrio et al. 1982; Martín et al. 1984; Fernández et al. 1996; García-Alix et al. 2008; García-Veigas et al. 2015; Fig. 2b). During the Quaternary, sedimentation concentrated in small, fault-controlled, high-subsidence depocenters (Morales et al. 1990; Rodríguez-Fernández and Sanz de Galdeano 2006; García-Alix et al. 2008), filled by detrital sediments (mostly conglomerates) (Fig. 2b).

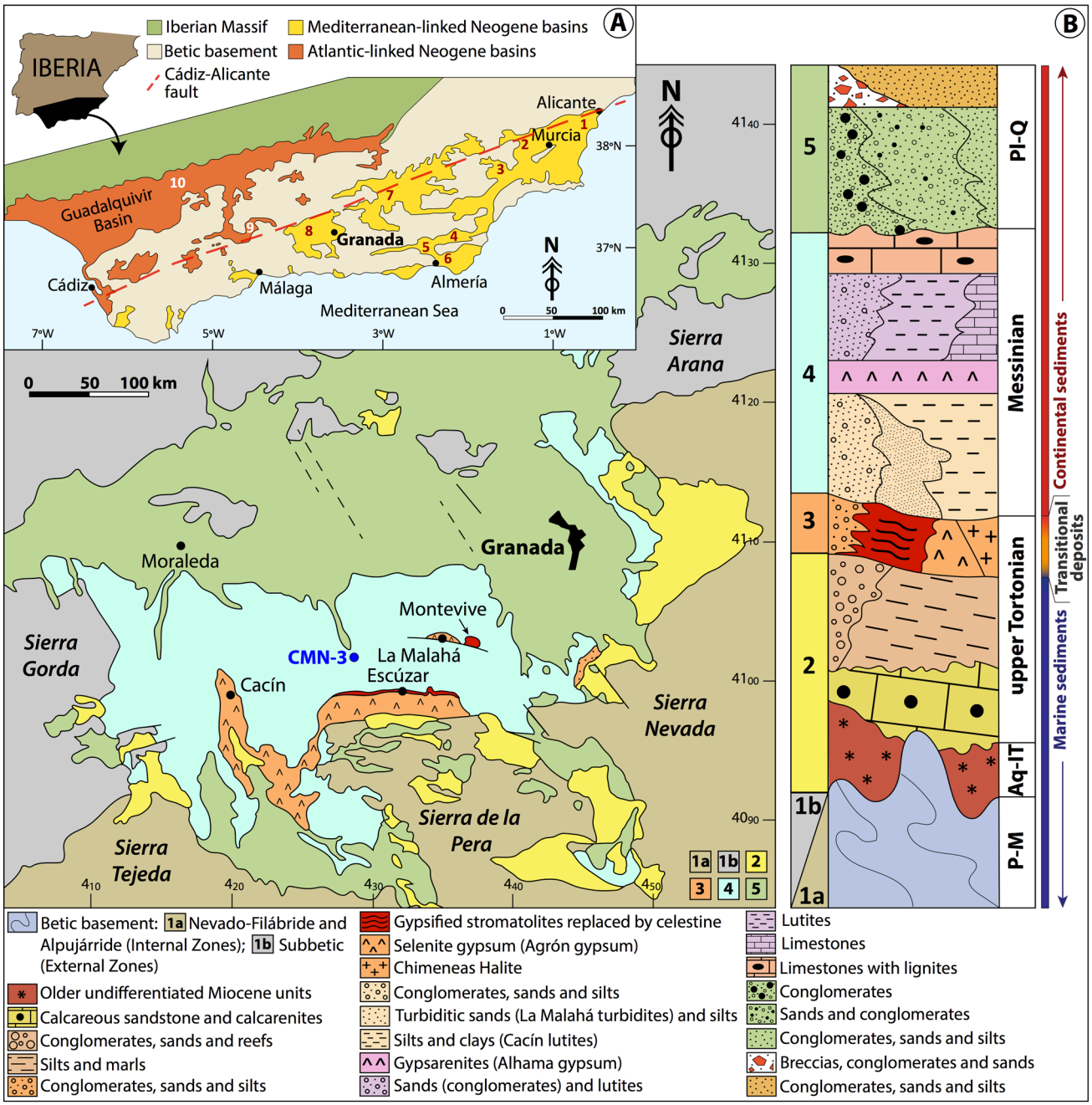

Fig. 2 Geological setting of the Granada Basin. (**a**) Major Neogene sedimentary basins of the Betic Cordillera, Spain. (1): Alicante-Bajo Segura Basin, (2): Fortuna Basin, (3): Lorca Basin, (4): Sorbas Basin, (5): Tabernas Basin, (6): Almería-Níjar Basin, (7): Guadix-Baza Basin, (8): Granada Basin, (9): Ronda Basin, (10): Guadalquivir Basin (from Braga et al. 2003). (**b**) Simplified geological map and Miocene to Quaternary stratigraphy of the Granada Basin (modified from Dabrio et al. 1982; Martín et al. 1984). Color code for the map is on the left side of the stratigraphic column. 1: Basement rocks; 2: Miocene marine deposits; 3: Miocene marine to continental, transitional (evaporite) deposits; 4: Miocene continental (lacustrine) deposits; 5: Pliocene–Quaternary continental (alluvial/fluvial) deposits. *P–M* Palaeozoic–Mesozoic; *Aq–lT* Aquitanian–lower Tortonian; *Pl–Q* Pliocene–Quaternary. Blue dot marks the position of the CMN-3 borehole

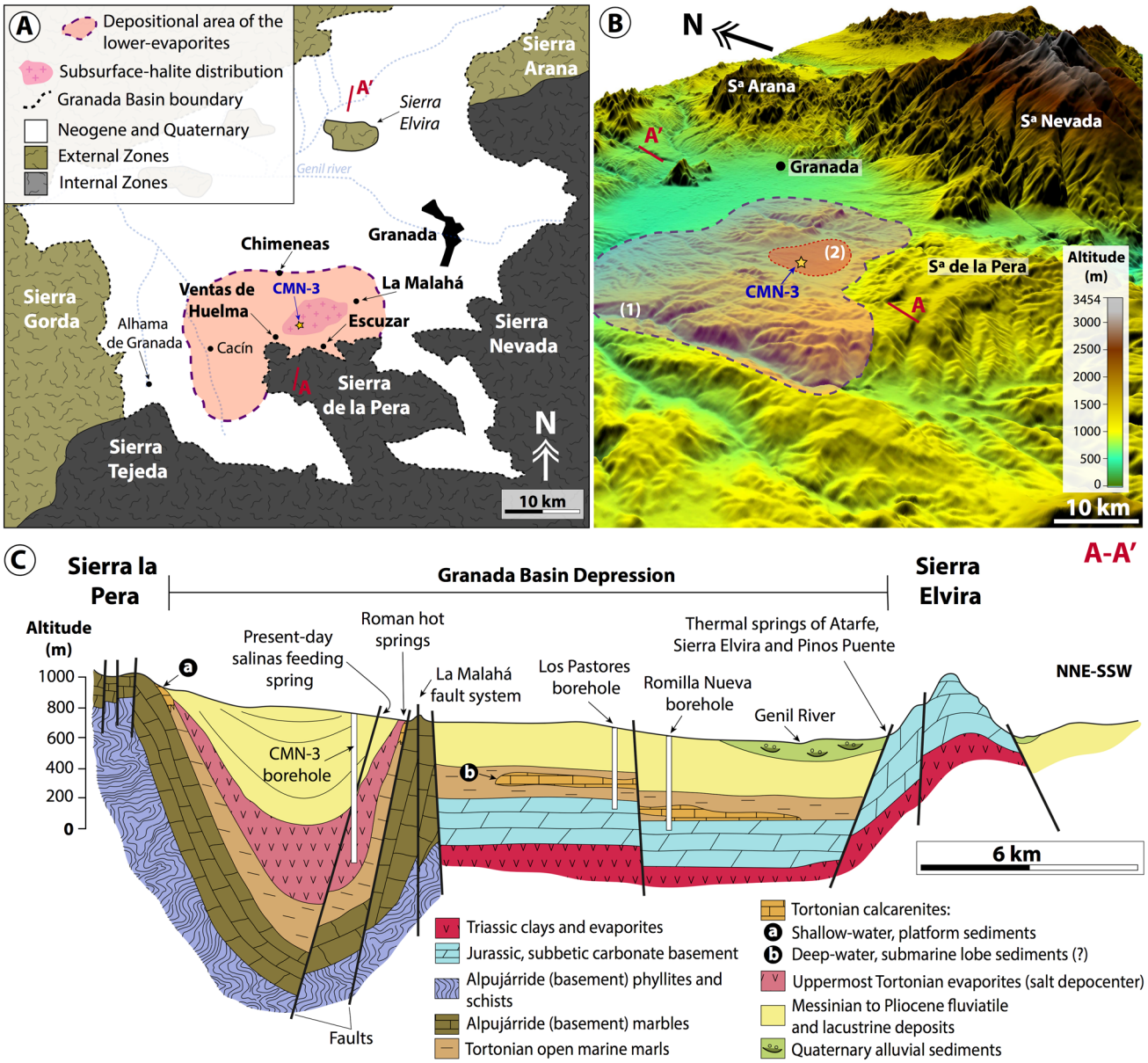

Fig. 3 Study area. **a** Simplified geological map of the Granada Basin and **b** detailed 3D topographic mosaic showing the location of the Lower Evaporites (sensu Dabrio et al. 1982) depositional area (1), and of the subsurface halite (2) (Chimeneas Halite, sensu García-Veigas et al. 2013, 2015). Note the position of the CMN-3 borehole (yellow star). Nearby villages are shown on the map. **c** Simplified geological cross-section of the Granada Basin and position of the salt depocenter (modified from Rosino 2008)

3 Materials and methods

3.1 Petrographic observations and facies analysis

This study concentrates on the ISU deposits drilled in the CMN-3 exploratory borehole, located close to the village of Ventas de Huelma (N 37°06′46.3″, W3°47′20.3″; Figs. 2, 3), in the Granada Basin. A detailed log of the ISU is shown in Fig. 4. Twenty-seven rock samples were taken from a 55-m-thick interval (at depths of 545–600 m).

Rock-facies analyses were based on visual (macroscopic) and microscopic (thin section) observations. Sixteen thin sections, about 30 µm thick, were prepared and impregnated by a blue epoxy (EpoBlue®) to distinguish pores from textural components. Thin sections were examined under polarized and cross-polarized light with a Nikon Eclipse LV 100 POL optical microscope. During the petrographic study, several image sequences were taken with a camera (ProgRes C10) connected to the microscope and captured with the ProgRes 2.1 image-management program.

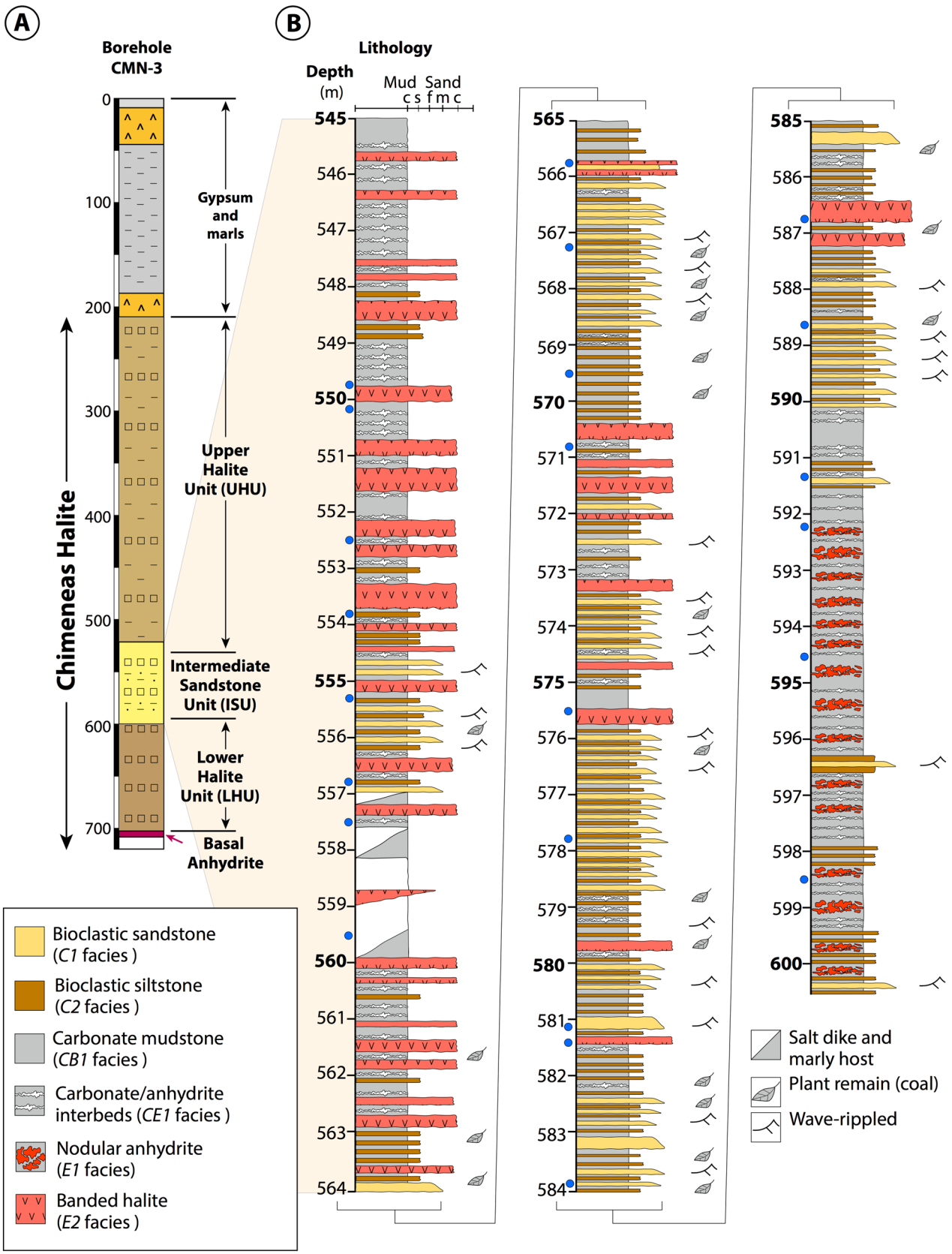

◂**Fig. 4** **a** Condensed lithological log of the CMN-3 borehole (after García-Veigas et al. 2013). **b** Detailed lithologic log of the Intermediate Sandstone Unit (ISU; CMN-3 borehole). Main lithologies, facies and sedimentary structures are shown. Blue dots indicate the position of the samples studied

3.2 Mineralogical and geochemical analyses

X-ray diffraction (XRD) was used to identify minerals as well as to determine the average bulk composition. For XRD determinations, 32 powders from ISU rocks were prepared with an agate mortar, and then analyzed with an X'pert PRO PW 3040/60 diffractometer operated at 50 kV, 30 mA. Samples were scanned in the 2θ range from 2° to 79°, with a step size of 0.033° (2θ)/s. The counting time was 120 min per sample.

SEM examinations were performed on two carbon-coated samples analyzed with a Zeiss Evo Ma 10 (10–15 kV beam current). Observations were carried out on backscattered electron image (BEI) mode, used to examine minerals that have initially been viewed and studied in conventional petrography, in order to gain information not available from the optical microscope.

Thirteen powders from discrete evaporite layers within the ISU were sampled with a dental drill (Dremel 225), in order to measure oxygen and sulfur stable-isotope composition ($\delta^{18}O_{SMOW}$ and $\delta^{34}S_{CDT}$). Contamination between two subsequently drilled samples was avoided by using diluted HCl to dissolve the carbonate components from the drill before each sampling. The isotope analysis was performed at the CCiT-UB (*Centres Científics i Tecnològics, Universitat de Barcelona*, Spain). To determine the isotope composition of the sulfate minerals (anhydrite), the samples were dissolved in > 18 $M\Omega\,cm^{-1}$ water, boiled, and recovered as $BaSO_4$ from a solution at pH ~ 3. The $\delta^{34}S_{CDT}$ was determined with a Carlo Erba 1108 elemental analyzer and the $\delta^{18}O_{SMOW}$ with a TC-EA unit, both coupled to an IRMS Thermo Finnigan Delta Plus XP. The analytical error (2σ) was ± 0.2‰ for $\delta^{34}S$ and ± 0.4‰ for $\delta^{18}O$ (values for standard NBS-127: $\delta^{34}S$ NBS-127: 20.3 ± 0.1‰; $\delta^{18}O$ NBS-127: 9.3 ± 0.2‰).

Four evaporite (halite and anhydrite) powders were sampled with a dental drill (Dremel 225), in order to measure strontium isotopic ratios ($^{87}Sr/^{86}Sr$). The same procedure as for the sampling of sulfate isotopes was followed to avoid contamination between subsequently drilled samples. The isotope analysis was performed at the SUERC (*Scottish Universities Environmental Research Centre*, Scotland, UK). The measurements were carried out on 1 mg of powder in a 2.5 M HCl. The separation between the two components was done by the standard procedure of ionic exchange. Samples were loaded onto single Re filaments and run on a VG Sector 54e thermal ionization mass spectrometer. The Sr ratio values were then normalized to a ratio value of $^{87}Sr/^{86}Sr = 0.1194$. The precision was better than ± 0.04‰.

4 Results

4.1 Facies description

The term 'facies' is broadly used to refer to a set of characteristics such as dimensions, sedimentary structures, grain size and type, color and biogenic content of a sedimentary-rock unit (Middleton 1973). The term 'evaporite facies' is used here in the same sense as in Schreiber and Kinsman (1975), Schreiber et al. (1976) or Aref et al. (1997) to refer to a evaporite sediment/sedimentary rock deposited under specific environmental conditions, regardless the age or physiographic–stratigraphic position.

Six ISU facies, organized in vertically stacked, cm- to dm-scale sequences throughout the study section (Fig. 4), have been recognized. They are classified into four groups: (1) clastic lithofacies; (2) carbonate lithofacies; (3) mixed, carbonate–evaporite lithofacies; and (4) evaporite lithofacies.

4.1.1 Clastic lithofacies

(a) Bioclastic sandstone (C1 facies): This facies consists of light to medium gray, moderately to well-sorted, fine- to coarse-grained bioclastic sandstones exhibiting an overall fining-upward trend (Fig. 5a). The bioclastic sandstone layers are up to 20 cm thick and intercalate between silts, carbonates, and evaporites (Fig. 4). Basal contacts are sharp and very irregular (Fig. 5b). This facies locally exhibits small (a few cm high) wave ripples (Fig. 5c) and wave-ripple cross lamination. Grains, ranging in size from 250 µm to 1 cm, are of carbonate bioclasts, plant remains, angular and highly irregular extraclasts (metamorphic and carbonate rocks), K-feldspar, quartz, and reworked evaporitic grains (Fig. 5d–i). Bioclasts, usually fragmented, are from bryozoans, bivalves, coralline algae, and foraminifera. Whole specimens of globigerinidae (*globigerines* and *globigerinoids*), *globoratalia* and other planktonic foraminifera (probably *orbuline*) are frequently found. Some whole specimens of benthic foraminifera (e.g. *miliolids* and *elphidium*) were also observed. Halite often occurs as intra- and inter-granular pore-filling cement (Fig. 5e, i).

(b) Bioclastic siltstone (C2 facies): This massive to banded, white to pale greenish-yellow silty facies occurs as tabular beds 0.5–15 cm thick, intercalated with bioclastic sands and carbonates (Figs. 4, 6a, b). Matrix consists of dense to pelloidal clay. Silt-sized grains are mainly from broken calcite, feldspar and quartz crystals, and minor dolomite and glauconite (Fig. 6c). Highly fragmented, fossil remains (mostly from planktonic foraminifera and bivalves) are also found (Fig. 6c,

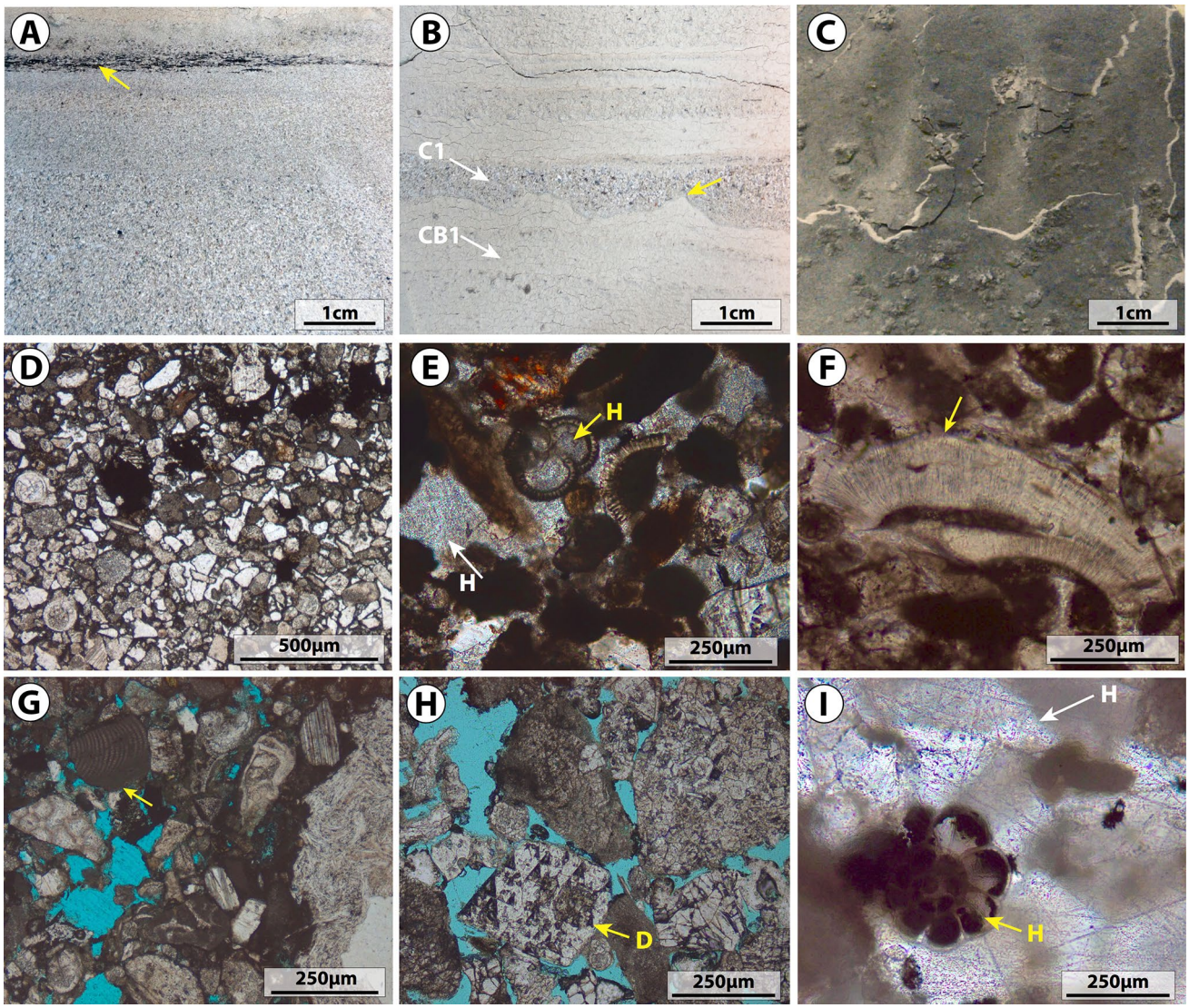

Fig. 5 Bioclastic sandstone (*C1* facies). **a** Core slab of a moderately to well-sorted, fine- to coarse-grained sandstone exhibiting an overall fining-upward trend. Plant remains (yellow arrow) concentrate on top. **b** Core slab of a thin, bioclastic sandstone layer (*C1*), intercalated between carbonate mudstones (*CB1*), exhibiting a highly irregular erosional base (yellow arrow). **c** Plan view showing poorly preserved wave ripples (aligned roughly parallel to the b axis of the picture) on top of a bioclastic sandstone layer. **d–i** Plain-polarized light (PPL) photomicrographs of the bioclastic sandstones. Grains, up to 1 cm in size, are of carbonate bioclasts (planktonic and benthic foraminifera, bryozoans, bivalves, and coralline algae), plant remains, quartz, K-feldspar, extraclasts (carbonate and metapelitic metamorphic rocks) and reworked evaporite minerals. Foraminifer shells are seen in **d** and **e**. A bivalve shell (yellow arrow), exhibiting a homogeneous prismatic wall structure, is shown in **f**. A coralline algal fragment (yellow arrow), exhibiting a series of light and dark bands and a cellular structure parallel to the long axis of the grain, can be found in **g**. Extraclasts are observed in **h**. They are metamorphic dolomite (yellow arrow) and metapelitic clasts from the Alpujárride Complex. **e** and **i** display intra- (yellow arrows) and inter-granular (white arrows) pore-filling halite cement. Remaining porosity is shown in blue

d). Plant debris (up to 0.6 cm in width and 2 cm in length) also occur (Fig. 6e, f). Halite is displayed as pore-filling cement.

4.1.2 Carbonate lithofacies: carbonate mudstone (CB1 facies)

This facies consists of light greenish-gray to dark brownish-green massive carbonate mudstone that intercalates with clastic and evaporite sediments (Figs. 4, 7a). Carbonate beds range in thickness from a few mm up to 10 cm. Calcite is the carbonate mineral, as determined by X-ray diffraction. Small anhydrite nodules, up to 1 cm in size, are locally found. Millimeter-sized, displacive halite crystals may also occur (Fig. 7a). Terrigenous components (calcite, feldspar and quartz grains, and clay minerals), if present, represent less than 15% of the rock bulk

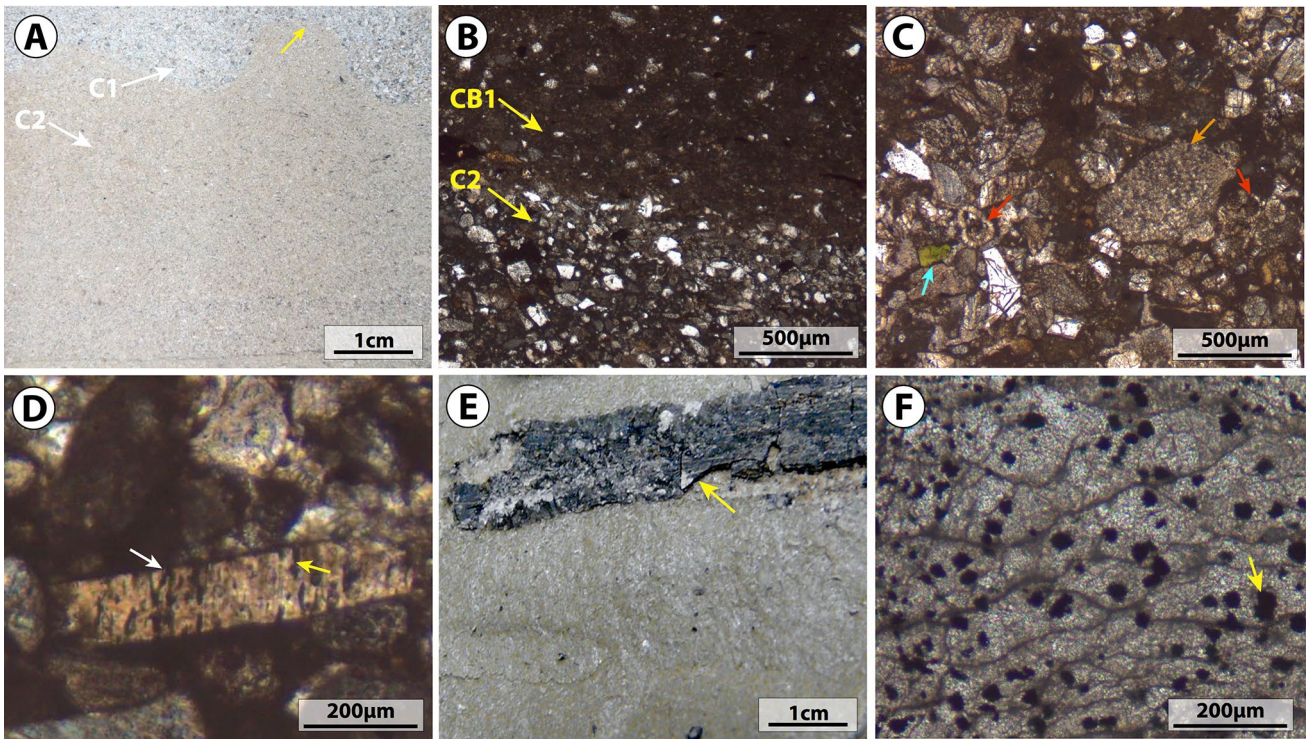

Fig. 6 Bioclastic siltstone (*C2* facies). **a** Core slab showing an erosive, sharp contact between *C1* and *C2* facies (yellow arrow). **b** PPL photomicrograph showing the contact between *C2* and *CB1* facies. **c** PPL photomicrographs showing main textural components of *C2* facies. Silt-sized grains are mainly from calcite, feldspar, quartz, carbonate bioclasts, and minor dolomite and glauconite (blue arrow). Carbonate bioclasts include fragments of coralline algae, bivalves, bryozoans (orange arrow) and foraminifera (red arrows). **d** PPL photomicrograph showing a bored, bivalve-shell fragment (white arrow). Borings (yellow arrow) are filled by carbonate mud (micrite). **e** Rock core sample (transversal section; view from above) of centimeter-sized plant debris (yellow arrow). **f** PPL photomicrograph showing pyrite particles (in black colour; yellow arrow) associated with plant debris

volume. Fossil remains, such as planktonic foraminifera and plant debris (Fig. 7b), and minor brachiopod/bivalve shell fragments, are locally found.

4.1.3 Mixed, carbonate–evaporite lithofacies: carbonate/anhydrite interbeds (CE1 facies)

This facies consists of an irregular alternation between light brownish-yellow carbonate mudstone bands, up to 3 cm thick, and white (cloudy) anhydrite laminae, ranging in thickness from < 1 mm to a few mm. The carbonate/anhydrite ratio is highly variable, although carbonate bands predominate. Lamination is commonly displayed as plane-parallel, tabular structures (Fig. 7c), but can also be wavy in shape (Fig. 7d). Anhydrite laminae show poorly delineated, ghost relics of presumably former micro-selenite gypsum crystals (Figs. 7e, f) and are made up of prismatic, disoriented lath crystals with a felted texture (e.g. Maiklem et al. 1969; Holliday 1973) (Fig. 7g, h).

4.1.4 Evaporite lithofacies

(a) Nodular anhydrite (E1 facies): This facies is composed of layers, up to 8 cm thick, made up of a mosaic of tightly packed, white anhydrite nodules, separated from one another by a light-brownish, carbonate mud matrix (Fig. 8a). Single nodules, ranging from a few mm to several cm in size, may exhibit a subtle, chicken-wire internal structure (e.g. Warren and Kendall 1985; Warren 2006, 2016). They consist of lath-shaped anhydrite crystal aggregates with a felted texture.

(b) Banded halite (E2 facies): This facies consists of small patches to centimeter- to decimeter-thick bands of intercalated white (cloudy) halite and gray halite (Fig. 8b, c). Contacts with enclosing clastic and carbonate facies (Fig. 4) are usually sharp. The fine to coarse, up to 1 cm in size, cloudy halite crystals exhibit a chevron structure and contain abundant fluid inclusions (Fig. 8c–e), whereas the coarse-grained, gray halite crystals are free of inclusions. The latter display an equigranular, mosaic-type texture (Fig. 8f). Carbonate mud commonly occurs interstitially

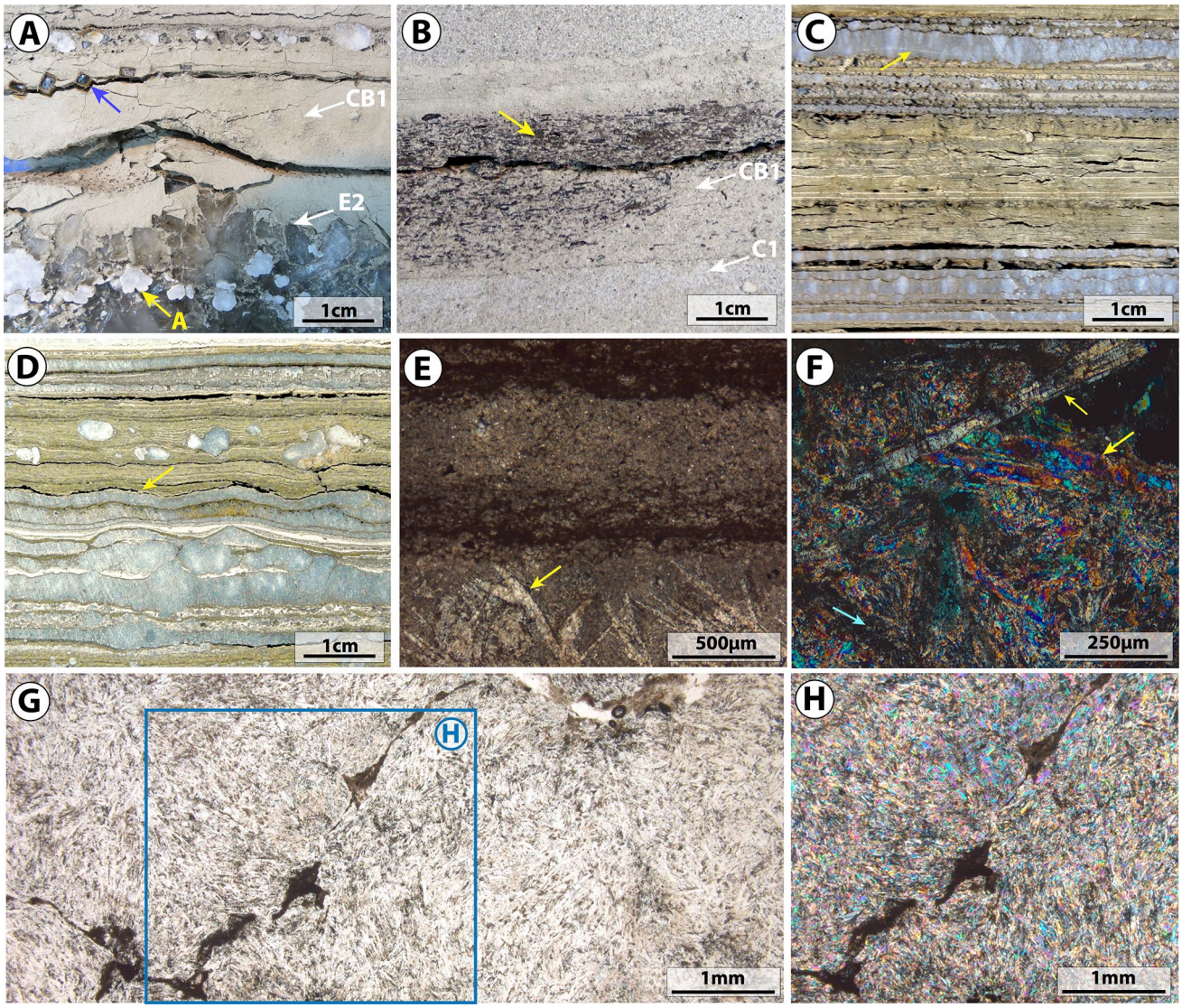

Fig. 7 Carbonate (*CB1*) and mixed, carbonate–evaporite (*CE1*) facies. **a** Core slab showing the contact between carbonate mudstone (*CB1*) and banded halite (*E2*) facies. Millimeter-sized, displacive halite crystals (blue arrow) are visible within *CB1* facies. Millimeter-sized anhydrite nodules (**a**), displaying an enterolithic-like structure, occur inside the halite bed (yellow arrow). **b** Core slab showing a carbonate mudstone layer (*CB1*) containing abundant plant debris (yellow arrow). **c**, **d** Core slabs showing carbonate-dominated lithofacies intercalating anhydrite laminae (yellow arrows) (*CE1* facies). Anhydrite laminae are often displayed as plane-parallel, tabular structures (as observed in picture **c**), but can also be wavy in shape (as reflected in picture **d**). **e** PPL photomicrograph showing ghost relics of presumably former micro-selenite gypsum crystals (yellow arrow) within a thin anhydrite lamina. **f** Cross-polarized light (*CPL*) photomicrograph showing in detail anhydrite-crystal pseudomorphs after micro-selenitic gypsum (yellow arrows) in *CE 1* facies. Anhydrite laminae display prismatic, disoriented lath crystals with a felted texture (blue arrow). **g**, **h** PPL and corresponding CPL photomicrographs showing anhydrite laminae (from *CE1* facies) made up of prismatic, disoriented lath crystals with a felted texture

filling in the space between cloudy halite crystals as well as filling in some fluid-inclusion voids (Fig. 8e, g). All this provides a chaotic, mottled appearance (also termed haloturbated texture, e.g. Smith 1971; Holdoway 1978) to the salt rock. Anhydrite nodules (up to 1 cm in diameter) concentrate at the base and the top of halite beds (Fig. 8f, h), often displayed as contorted bands of coalesced nodules (enterolithic-like structures; e.g. Shearman and Fuller 1969; Warren and Kendall 1985; Warren 2006, 2016). Anhydrite nodules are made up of lath-shaped crystals with a felted texture.

4.2 Facies distribution

With respect to lithofacies distribution, a series of intervals can be clearly distinguished in the ISU sequence from bottom to top. The first interval (from 601 to 592 m deep; Fig. 4) is characterized by the predominance of

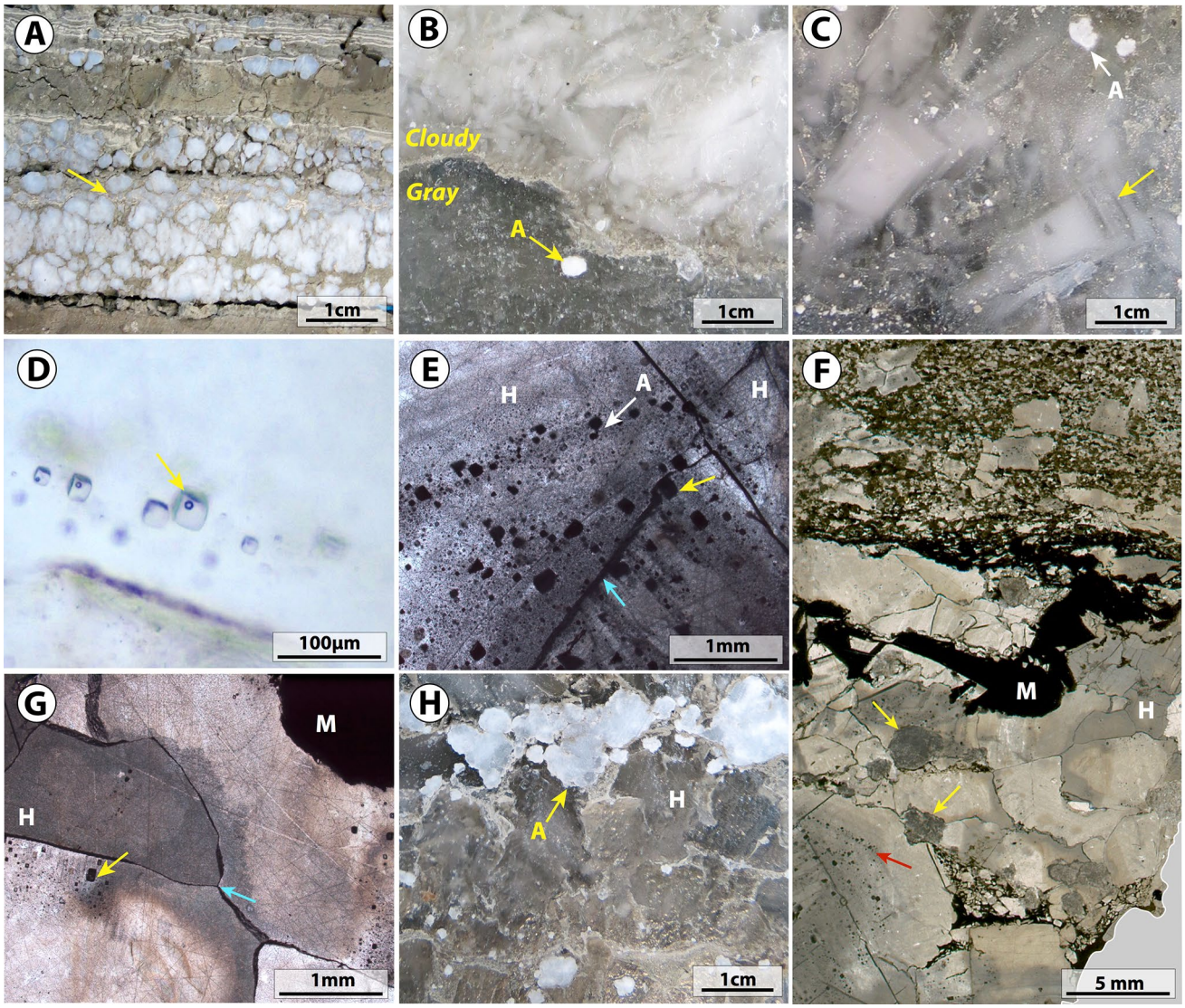

Fig. 8 Nodular anhydrite (*E1*) and banded halite (*E2*) facies. **a** Core slab showing a mosaic of tightly packed, white anhydrite nodules separated from one another by a carbonate matrix (*E1* facies; yellow arrow). **b** Core slab displaying irregular bands of white (cloudy) primary halite and gray mosaic-type, secondary halite (*E2* facies). Millimeter-sized anhydrite nodules (yellow arrow) occur within the mosaic-type halite. **c** Core slab showing relics of primary, cloudy halite crystals (yellow arrow), exhibiting a chevron structure, inside patches of secondary, mosaic-type halite. **d** PPL photomicrograph showing biphasic, fluid inclusions (yellow arrow) inside a primary, white (cloudy) halite crystal. **e** PPL photomicrograph showing a close view of the rows or clusters of fluid inclusion voids (yellow arrows), filled by carbonate mud. Carbonate mud also fills the interstitial space between halite crystals (blue arrows). **f** High-resolution image of a scanned thin section showing upper contact of *E2* facies. Mosaic-type halite (H), millimeter-sized anhydrite nodules (yellow arrows), interstitial carbonate mud between halite grains (M), as well as remains of chevron structures (as rows or clusters of fluid inclusion voids; red arrow), are indicated. **g** PPL photomicrograph showing equigranular, mosaic-type replacement halite. Note curved crystal boundaries meeting at triple junctions (blue arrow). Rows or clusters of fluid-inclusion voids, filled by carbonate mud (yellow arrow), delineate the shape of the former, primary-halite crystal. **h** Core slab showing coalesced anhydrite nodules, display as contorted bands (enterolithic-like structures; yellow arrow), accumulated at the top of a halite band

nodular anhydrite layers (*E1* facies) and carbonate mud (*CB1* facies). In the second interval (from 592 to 564 m deep; Fig. 4) clastic sediments (*C1* and *C2* facies), locally intercalating halite (*E2* facies) and carbonate/anhydrite interbeds (*CE1* facies), are dominant. In the third interval (from 564 to 545 m deep; Fig. 4) evaporites, halite (*E2* facies), and carbonate/anhydrite interbeds (*CE1* facies), are the most abundant deposits.

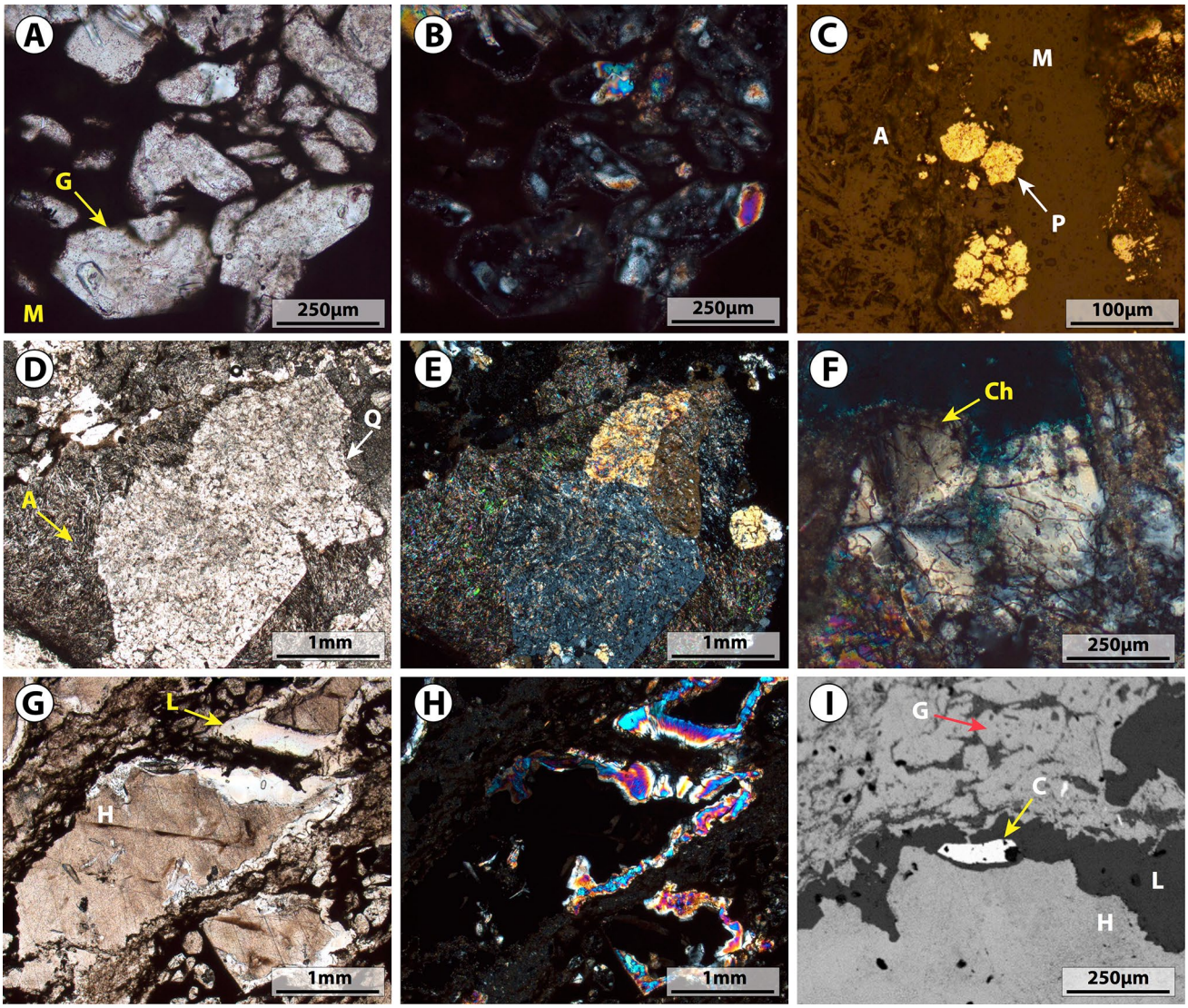

Fig. 9 Other mineral occurrences. **a**, **b** PPL and corresponding CPL photomicrographs showing lenticular to prismatic gypsum crystals, now preserved as halite pseudomorphs (yellow arrow), embedded in carbonate mud (M). **c** Reflected light microscope (RLM) photomicrograph showing micron-sized pyrite framboids (in yellow colour; white arrow) within carbonate mud. **d**, **e** PPL and corresponding CPL photomicrographs showing partial replacement of an anhydrite nodule (yellow arrow) by equigranular quartz (megaquartz; white arrow). Relicts of the felted anhydrite texture can still be recognized in the quartz. **f** CPL photomicrograph showing replacement of pre-existing evaporites (i.e. halite and anhydrite) by zebraic chalcedony (yellow arrow). **g**, **h** PPL and corresponding CPL photomicrographs showing selected replacement of mosaic-type halite by lutecite at grain boundaries (yellow arrow). **i** SEM photomicrograph (BSD) showing replacement of mosaic-type halite (H) by lutecite (L), which in turn was replaced by celestine (C; yellow arrow). Gypsum crystals, now preserved as halite pseudomorphs (G; red arrow), are also visible

4.3 Additional petrographic observations: other mineral occurrences

4.3.1 Gypsum ($CaSO_4 \cdot 2H_2O$)

Gypsum occurs as single, lenticular to prismatic crystals, up to 150 µm in width and 400 µm in length (Fig. 9a, b), preserved as halite pseudomorphs. It is common at the base of some halite beds.

4.3.2 Pyrite (FeS_2)

Pyrite occurs as framboid crystals, up to 100 µm in size, within the carbonate and clastic lithofacies (Fig. 9c), commonly associated with plant debris (Fig. 6f).

4.3.3 Authigenic silica (SiO_2)

Authigenic silica occurs as equigranular quartz (megaquartz) and fibrous quartz (zebraic chalcedony and lutecite) replacing evaporites, mainly halite and anhydrite. Equigranular quartz consists of euhedral, equant crystals (> 20 µm; megaquartz) within which felted anhydrite relicts are preserved (Fig. 9d, e). Chalcedony consists of sheaf-like bundles of radial, length-fast fibers of quartz, in which the crystallographic *c*-axis lies normal to fiber long axis. Low birefringence yields first-order white/gray/yellow interference colors. Spherulitic growth with maltese-cross or zebraic extinction is observed in chalcedony (Fig. 9f). Lutecite consists of length-slow fibers of quartz (i.e. chalcedony), in which *c*-axis is oriented at approximately a 30° angle to the long axis of the fiber. High birefringence, second-order yellow/magenta/blue interference colors were observed in lutecite (Fig. 9g–i).

4.3.4 Celestine ($SrSO_4$)

Celestine occurs in very minor quantities as individual, µm- to mm-sized crystals, associated with halite. This mineral was identified under scanning electron microscope (SEM; Fig. 9i), presenting a white color and lenticular morphologies.

4.4 Isotope data

4.4.1 Sulfate isotopes ($\delta^{34}S$ and $\delta^{18}O$)

Sulfur and oxygen isotope values from the ISU at the CMN-3 borehole are listed in Table 1 and plotted as $\delta^{18}O_{V\text{-}SMOW}$ vs. $\delta^{34}S_{V\text{-}CDT}$ in Fig. 10. For comparison, values are also shown from the Granada Basin (Chimeneas Halite Succession; García-Veigas et al. 2013) and other Iberian Peninsula Miocene basins (Calatayud, Tajo, and Ebro basins; Utrilla et al. 1992), along with values for Miocene marine sulfates (from Claypool et al. 1980; Paytan et al. 1998), upper Triassic gypsum deposits (Keuper; García-Veigas et al. 2013) and Tortonian gypsum deposits (Rouchy and Pierre 1979).

The $\delta^{34}S_{V\text{-}CDT}$ values from the ISU range from + 10 to + 20.9‰ with an average of +18.5 ± 1.9‰ (Fig. 11). The lowest value (+ 10‰) was found in a nodular-anhydrite sample rich in pyrite. All these values are lower than those estimated for Miocene marine sulfates ($\delta^{34}S$: + 21 to + 24‰; Paytan et al. 1998) and higher than those recorded from upper Triassic gypsum outcropping in the Granada Basin (+14.3 ± 0.7‰; García-Veigas et al. 2013), with the exception found at 556.8 m deep (nodular-anhydrite sample rich in pyrite). Some of these values are also comparable to those reported for the Tortonian gypsum from the Granada Basin (+16.7 ± 0.7‰; Rouchy and Pierre 1979).

Table 1 Geochemistry-analysis results of ISU samples: sulfate isotope composition ($\delta^{18}O_{V\text{-}SMOW}$; $\delta^{34}S_{V\text{-}CDT}$), and $^{87}Sr/^{86}Sr$ isotope ratios

Depth (m)	$\delta^{18}O$ (‰)	$\delta^{34}S$ (‰)	$^{87}Sr/^{86}Sr$	Source
Upper Halite Unit—UHU				
382	16.2	17.2		García-Veigas et al. (2013)
391.4			0.708710	García-Veigas et al. (2013)
413.2	15.1	16.8		García-Veigas et al. 2013
489	14.9	16.5	0.708706	García-Veigas et al. (2013)
514.6			0.708795	García-Veigas et al. (2013)
529.6	15.4	17.5	0.708707	García-Veigas et al. (2013)
Intermediate Sandstone Unit—ISU				
553.7	14.8	16.4		This study
555	15.5	17.9	0.708771	This study
556.8	12.8	10		This study
559.5	15.6	18.1		This study
565.7	15.5	16.1	0.708710	This study
567.2	15.8	20.1		This study
569.5	16.4	20.3		This study
575.9	16	19.5	0.708779	This study
577	16.1	19.1		García-Veigas et al. (2013)
581.4	16.4	20.9		This study
581.4	16.2	20		This study
584.2	15.8	18.7		This study
584.7	14.7	14.8		This study
586.8	15.9	20.1	0.708723	This study
586.9			0.708717	García-Veigas et al. (2013)
Lower Halite Unit—LHU				
617.6	13.6	16.3		García-Veigas et al. (2013)
638	12.3	16		García-Veigas et al. (2013)
648.1			0.708735	García-Veigas et al. (2013)
659.5	11.9	17.1		García-Veigas et al. (2013)
678.4	12.5	17.7		García-Veigas et al. (2013)
703.5	15.1	17.3		García-Veigas et al. (2013)
720	13.4	21		García-Veigas et al. (2013)
724.1	12.8	21.7	0.708807	García-Veigas et al. (2013)
Basal anhydrite bed				
730	13.5	23.6	0.708869	García-Veigas et al. (2013)

Isotope values reported by García-Veigas et al. (2013) for the basal anhydrite bed, and the LHU, ISU, and UHU, respectively, are also shown for comparison

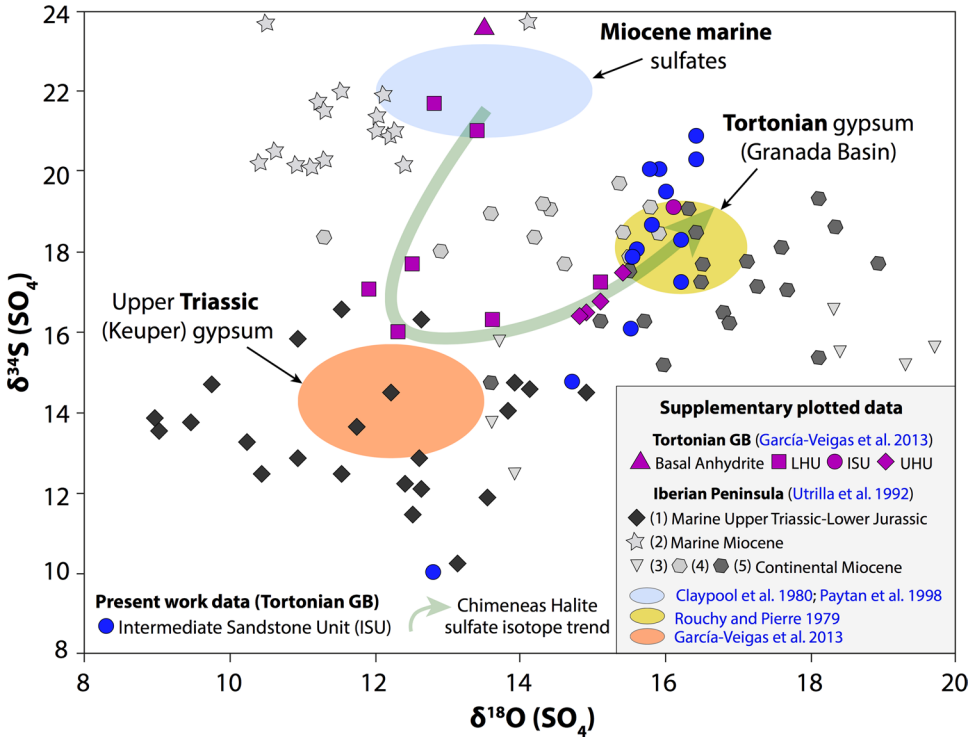

Fig. 10 A scatter plot of $\delta^{18}O$ and $\delta^{34}S$ values of the evaporite (sulfate) ISU of the Chimeneas Halite Succession at the CMN-3 borehole. Data are completed for comparison with values from the Granada Basin (Chimeneas Halite Succession; García-Veigas et al. 2013; sulfate isotope trend: green arrow) and other Iberian Peninsula Miocene basins (Calatayud, Tajo, and Ebro basins; Utrilla et al. 1992), along with values for Miocene marine sulfates (from Claypool et al. 1980; Paytan et al. 1998), Upper Triassic gypsum deposits (Keuper; García-Veigas et al. 2013) and Tortonian gypsum deposits (Rouchy and Pierre 1979)

The $\delta^{18}O_{V\text{-}SMOW}$ values from the ISU range from + 12.8 to + 16.4‰ with an average of +15.7 ± 0.5‰ (Fig. 11). The lowest value (+ 12.8‰) was found in a sample taken at 556.8 m deep. ISU samples have $\delta^{18}O_{V\text{-}SMOW}$ signatures higher than those of Miocene marine sulfates ($\delta^{18}O$: + 12 to + 14‰; Claypool et al. 1980) and also higher than those recorded from upper Triassic gypsum outcropping in the Granada Basin (+12 ± 0.5‰; García-Veigas et al. 2013). The values are also comparable to those reported for Tortonian gypsum deposits from the Granada Basin (+16.8 ± 0.5‰; Rouchy and Pierre 1979).

4.4.2 Strontium isotope ratios ($^{87}Sr/^{86}Sr$)

Strontium isotope analysis ($^{87}Sr/^{86}Sr$ ratios) for several anhydrite nodules and halite samples from the ISU of the CMN-3 borehole are listed in Table 1. The data are compared with $^{87}Sr/^{86}Sr$ values of Triassic dolomite (Gorzawski et al. 1989) and Triassic evaporites (Ortí et al. 2014b) from the Betic Cordillera, and from the Tortonian seawater (Hodell et al. 1991) in Fig. 11.

The $^{87}Sr/^{86}Sr$ ratio ranges from 0.708710 to 0.708779 with an average of 0.708745, which is slightly higher compared with the values reported for the ISU and UHU by García-Veigas et al. (2013) (~0.708710; Table 1). These values are lower than the Tortonian seawater $^{87}Sr/^{86}Sr$ ratio (~0.7089, Hodell et al. 1991) and higher than the $^{87}Sr/^{86}Sr$ ratio measured in Triassic dolomite (~0.70825; Gorzawski et al. 1989) and evaporite (0.707615–0.708114; Ortí et al. 2014b) samples from the Betic Cordillera.

5 Interpretations and discussion

5.1 Facies interpretation and environment of deposition

In the ISU, six major lithofacies occur: (a) bioclastic sandstones (*C1*); (b) bioclastic siltstones (*C2*); (c) carbonate mudstones (*CB1*); (d) carbonate/anhydrite interbeds (*CE1*); (e) nodular anhydrite (*E1*), and (f) banded halite (*E2*).

The bioclastic sandstones (*C1*) have a clearly marine provenance as testified to by the presence of abundant, sometime well-preserved carbonate bioclasts, including bryozoans, bivalves, coralline algae, and foraminifera. This biota association is commonly found in temperate-water, carbonate-platform deposits and is well exemplified in sediments of this age (uppermost Tortonian) from the nearby Almería basins (Sorbas and Vera basins and Cabo de Gata area) (Martín et al. 1996, 2010; Betzler et al. 1997; Braga et al. 2006; Puga-Bernabéu et al. 2007). Centimeter-thick (3–20 cm), sandstone layers are relatively well sorted, exhibit a very irregular, clearly erosive base (Fig. 5b), and show a fining-upward grading (Fig. 5a) and small (cm-sized), wave-ripple and wave-ripple cross lamination on top (Fig. 5c). They are interpreted as storm layers, reworked by very gentle waves, that were deposited in a very shallow

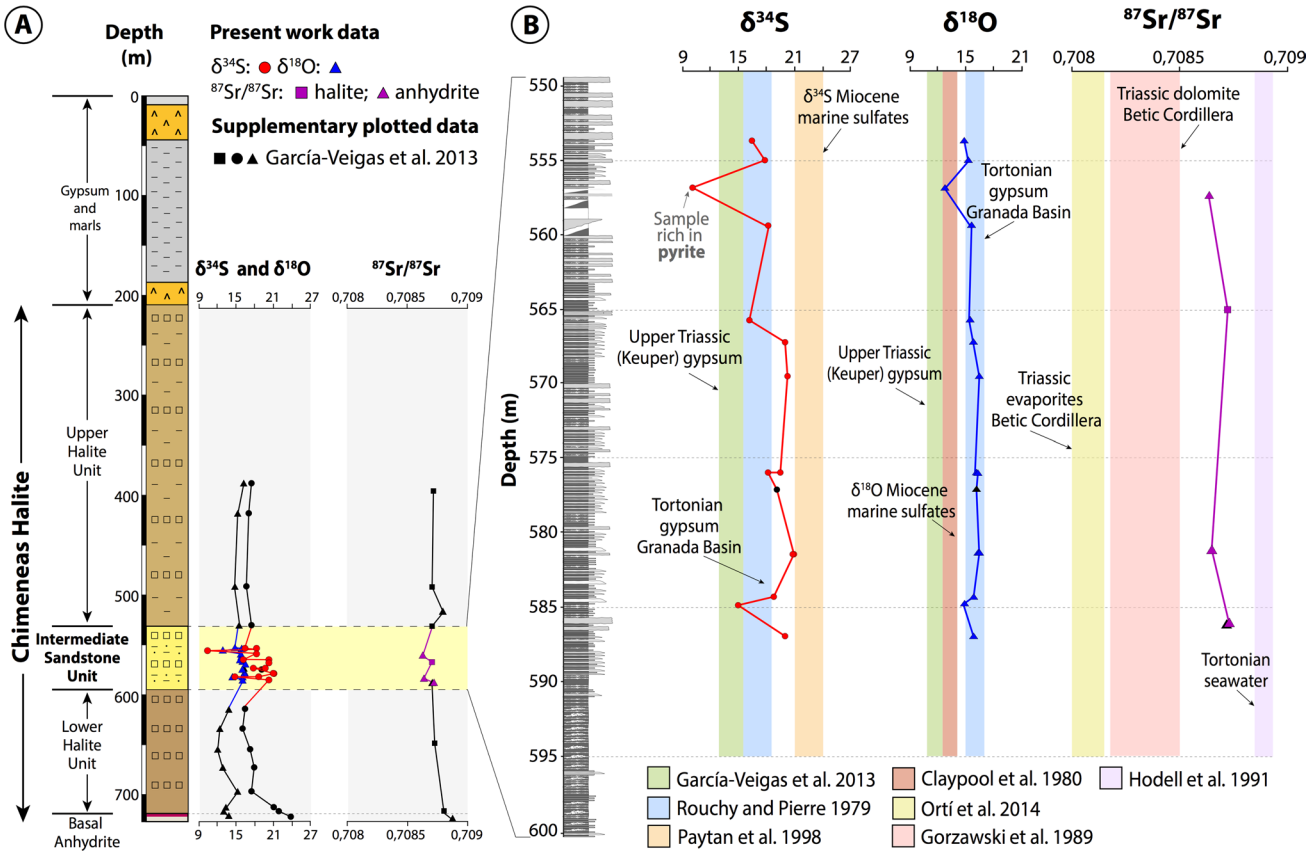

Fig. 11 **a** Condensed geochemical evolution of the Chimeneas Halite (CMN-3 borehole). Sulfate isotope composition ($\delta^{18}O$ and $\delta^{34}S$) and $^{87}Sr/^{86}Sr$ ratio data come from García-Veigas et al. (2013) and from this work (ISU interval). **b** Vertical evolution of geochemical profiles ($\delta^{34}S$, $\delta^{18}O$ and $^{87}Sr/^{86}Sr$) of the ISU of the Chimeneas Halite Succession at the CMN-3 borehole. Sulfate isotope values for the ISU (this work) are compared with those from Miocene marine sulfates ($\delta^{18}O$ from Claypool et al. 1980, $\delta^{34}S$ from Paytan et al. 1998), Upper Triassic (Keuper) gypsum deposits (García-Veigas et al. 2013) and Tortonian gypsum deposits from the Granada Basin (Rouchy and Pierre 1979). Strontium isotope ratios (this work) are compared with $^{87}Sr/^{86}Sr$ values of Triassic dolomite (Gorzawski et al. 1989) and Triassic evaporites (Ortí et al. 2014b) from the Betic Cordillera, and Tortonian seawater (Hodell et al. 1991)

barrier coastal lake. Similar deposits have been described by Warren and Kendall (1985), Warren (1991), Evans (1995), Kirkham (1997) and Strohmenger et al. (2011) in the Arabian (Persian) Gulf. In the study example, terrigenous grains are mainly dolomitic and metapelitic, high-grade metamorphic clasts indicating an Alpujárride source. Clast composition suggests they derived from some locally emerging reliefs located to the S–SW of the salt depocenter (Fig. 3), at the position of the present-day Sierra de la Pera and Sierra Tejeda where these types of rocks crop out extensively today (Aldaya et al. 1980).

Bioclast remains in the siltstones (*C2*) indicate a marine provenance as well. These sediments were also introduced in the coastal lake during storms but, due to their small particle size, remained for a time in suspension before being deposited.

Carbonate mudstone (*CB1*), calcitic in composition, is considered to be the result of chemical precipitation within the coastal lake. It may locally incorporate some allochthonous, terrigenous/bioclastic silt grains as well as some clay.

Anhydrite growths, closely associated with the carbonate mudstones, occur in two ways, either as thin (< 1 mm to a few mm thick), anhydrite laminae intercalated within carbonate mudstones (*CE1* facies) (Fig. 7c, d), or as layers (up to 8 cm thick) made up of a mosaic of tightly packed nodules (*E1* facies) (Fig. 8a). Anhydrite laminae (in *CE1* facies) formed by the replacement of thin, selenite-gypsum levels. As stated above, they show ghost relics of presumably former micro-selenite gypsum crystals (Fig. 7e, f). Anhydrite nodules (*E1* facies) exhibit a subtle, chicken-wire internal structure. This sort of structure has been described in modern marine and continental evaporitic sabkha, where anhydrite, crystallizing from interstitial hypersaline waters inside the mud, results from synsedimentary transformation after gypsum (e.g. Warren 2006, 2016). High temperatures (~ 35–45 °C) at shallow (1–2 m) depths can lead to the conversion from gypsum to anhydrite in the near-surface when

pore-fluid salinity is close to halite saturation (Warren 2016). According to Holser (1979), in evaporitic settings dominated by gypsum and halite, anhydrite replacement can occur at 25 °C. Such temperatures are common on modern evaporitic playas and could have been reached in the Granada Basin in the latest Tortonian. Anhydrite-nodule formation took place within the carbonate mud in the saline lake by the replacement of previously formed gypsum crystals.

Primary halite (in *E2* facies) consists of centimeter- to decimeter-thick strata of massive, white (cloudy) halite, exhibiting a chevron structure (Fig. 8c) and containing abundant, sometime aligned, fluid inclusions (Fig. 8d, e). Halite crystals are up to 1 cm in size. This halite was deposited at times when the coastal lake turns into a fully saline lake. Lenticular to prismatic gypsum crystals occurring at the base of some halite layers are interpreted as having precipitated during the first stages of concentration in the saline lake. Chevron fabric in salt is interpreted as forming by competitive growth of bottom-nucleated (subaqueous) crystals (e.g. Lowenstein and Hardie 1985). Relict zones of chevron growth fabrics outlined by brine inclusions are the most common primary texture preserved in modern and ancient salt deposits (e.g. Hardie 1984; Lowenstein and Hardie 1985; Schléder and Urai 2005).

From facies interpretation it is inferred that the deposition environment for the whole ISU was that of a coastal lake,

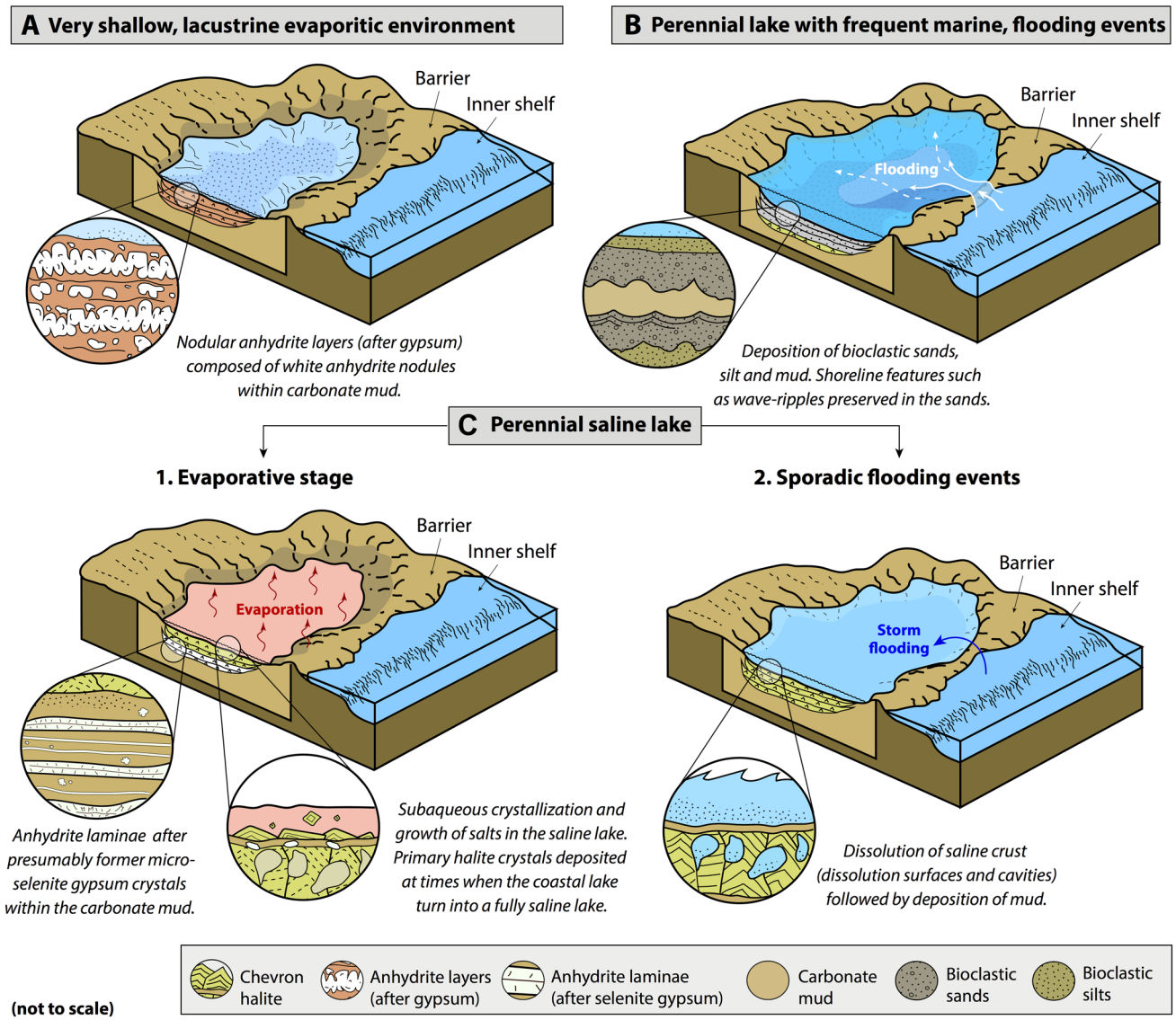

Fig. 12 Major stages in the temporal evolution of the coastal lake during deposition of the ISU. **a** Synsedimentary formation of the nodular anhydrite beds (after gypsum) within carbonate mud in a very shallow, lacustrine evaporitic environment. **b** Persistent marine influence and frequent inundation of the lake during major storms with deposition of bioclastic sands and silts. **c** Perennial saline lake with precipitation of micro-selenite gypsum and halite. Sporadic inundations resulted in the partial dissolution of some of the halite layers

more likely isolated from the open sea by a sand barrier, subjected to strong salinity fluctuations.

5.2 Coastal-lake evolution

As pointed out above, vertical facies distribution in the ISU sequence shows three distinct intervals (Fig. 4). At the bottom of the sequence (first interval) nodular anhydrite layers are frequently found. In the middle (second interval) bioclastic sediments are dominant. At the top (third interval) halite layers and carbonate/anhydrite interbeds are ubiquitous.

These intervals in turn mark three different stages in the temporal evolution of the lake (Fig. 12). Syn-depositional anhydrite nodules formed close to surface in a very shallow, lacustrine evaporite environment (stage 1, Fig. 12a). Stage 1 is considered to be the shallowest in the lake's evolution. The environmental change was then to a deeper, perennial lake undergoing frequent marine flooding storm events resulting in bioclastic deposition (stage 2, Fig. 12b). A shallower, perennial saline lake was finally established (stage 3, Fig. 12c), with major evaporite (anhydrite and halite) formation. Anhydrite laminae are thought to be the result of replacement of bottom-nucleated (subaqueous), micro-selenite gypsum. Chevron halite beds resulted from the precipitation and competitive growth of bottom-nucleated, salt crystals.

Marine flooding events resulted in partial dissolution of the primary halite crust. Dissolution concentrated at first at grain boundaries (e.g. Shearman 1970), creating later larger, elongated cavities. Dissolution of the saline crust was followed by the deposition of a thin, carbonate-mud lamina (Fig. 13), precipitated from the brackish water resulting from the incorporation of under-saturated water immediately after the flooding event.

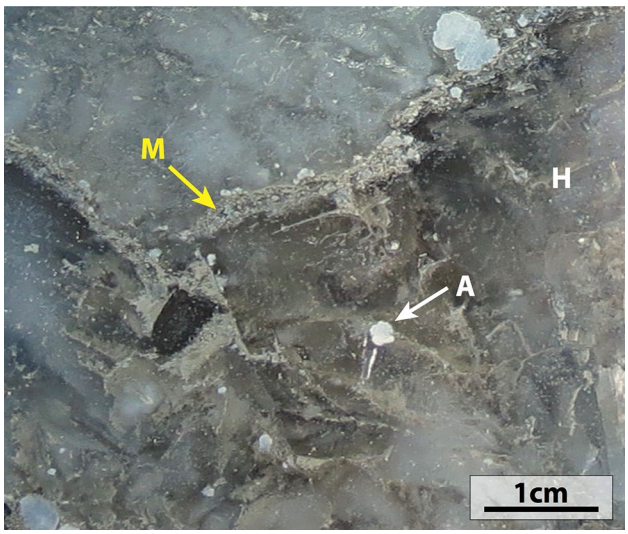

Fig. 13 Core slab showing dissolution on the topmost part of a halite layer (H). Dissolution was followed by the deposition of a thin, carbonate-mud lamina (M, yellow arrow), which occurs now lining the former dissolution surface. White arrow points to a small anhydrite (A) nodule

The Granada Basin saline lake thus experienced repeated periods of flooding (and partial dissolution of evaporites), and of salt crystallization (Fig. 12c). Syn-depositional textures recorded in recent salt-pans (e.g. Shearman 1970; Lowenstein and Hardie 1985; Casas and Lowenstein 1989), which have also been reported in ancient salt deposits (e.g. Wardlaw and Schwerdtner 1966; Casas and Lowenstein 1989; Benison and Goldstein 2001; Schléder and Urai 2005), are consistent with our interpretations for the ISU. Salt-pan evolution normally shows repeated periods of flooding, evaporative concentration and, sometimes, desiccation. The flooding stage incorporates unsaturated floodwaters into the salt-pan, converting it into a temporary shallow brackish lake. As reported by many authors, both fresh- and marine-water flooding events are frequent in marginal-marine, saline pans (e.g. Lowenstein and Hardie 1985; Schreiber and El Tabakh 2000; Benison and Goldstein 2001; Warren 2006, 2010, 2016). Fresh waters typically come from rainstorm runoff (and snow meltwater), while seawaters are washed onto the pan by storm floods and, rarely, at high spring tides. In our example, the absence of desiccation structures (mud cracks, tepees, etc.) indicate that 'the saline pan cycle' in the sense of Lowenstein and Hardie (1985) was never completed up to the point of full desiccation of the coastal, saline lake.

5.3 Diagenetic evolution

The petrographic study shows the effect of several diagenetic processes, taking place at different times (stages), after sediment deposition, in the course of the diagenesis (Fig. 14).

5.3.1 Syn-depositional diagenetic stage

As discussed above, anhydrite is replacing former gypsum crystals in nodules (*E1* facies) and layers (*CE1* facies) within the carbonate mudstone. These anhydrite replacements are thought to have occurred very early, within the deposition environment. Dissolution surfaces developed on top of halite layers after flooding events. Brackish waters were responsible for this dissolution (dissolution stage 1, herein). Dissolution cavities also developed underneath, inside the salt (Figs. 13, 15a). Clear halite, precipitated as void-filling cement inside primary-halite, dissolution cavities, exhibits no preferred crystal orientation, growth direction or elongation. This halite, which often truncates the chevron halite crystals, is interpreted as newly formed, synsedimentary cement precipitated from interstitial groundwater brines (e.g. Shearman 1970; Lowenstein and Hardie 1985; Casas and Lowenstein 1989). This limpid, clear halite also occurs

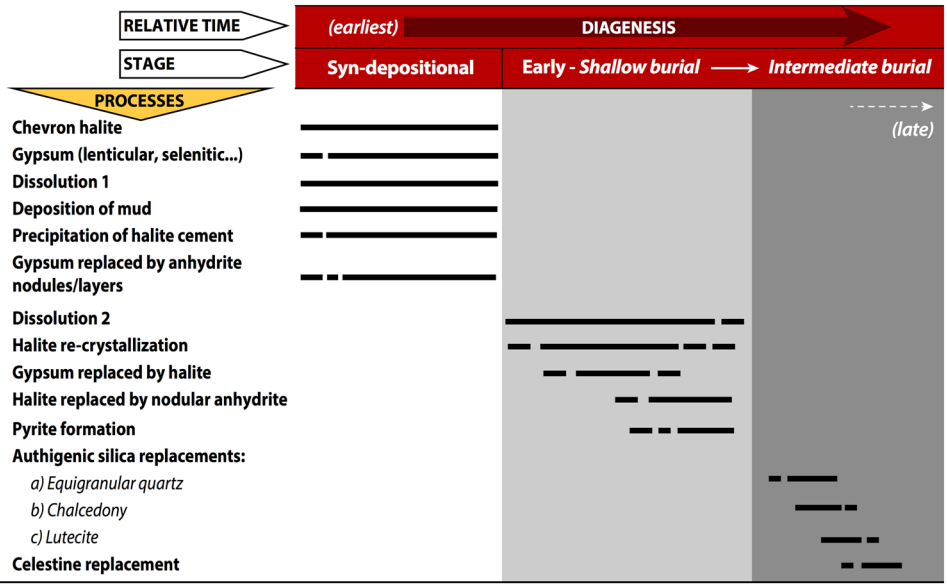

Fig. 14 ISU sequence of diagenetic events (CMN-3 borehole)

as intra- and inter-granular pore-filling cement (Fig. 5e, i) in underlying clastic facies.

5.3.2 Early diagenetic stage

Early diagenesis is reflected in the halite deposits (*E2* facies) by re-crystallization processes, back reactions, and replacements. The main early diagenetic process is halite re-crystallisation of pre-existing halite (depositional primary halite and syn-depositional halite cement) (Fig. 8b, c), as a result of repetitive dissolution (dissolution stage 2)-precipitation cycles (Fig. 15b). Recrystallized halite shows up as an equigranular mosaic, in which the curved crystal boundaries meet at triple junctions with angles of approximately 120° (Fig. 8g). The fact that this mosaic-type halite exhibits dissolution gulfs like those described in the primary, depositional halite, and that it sometimes fills in intergranular pores in the immediately underlying sandy and silty layers (*C1* and *C2* facies), points to an early diagenetic process occurring close to surface. According to Lowenstein and Hardie (1985) and to Warren (2016), dissolution and re-crystallization of primary halite into a secondary halite occurs under a few cm to meters of burial depth from brine reflux following the dissolution of the primary halite. In our example the reflux brines seem to have moved preferentially along bedding planes since re-crystallization locates preferentially at the base and on top of the halite layers, resulting in their final banding display. Early re-crystallization processes derived from repetitive dissolution–precipitation processes have been reported in desiccated halite-floored salinas and salt lakes (e.g. Handford 1982).

Halite replacement of gypsum is shown by gypsum pseudomorphs keeping external morphologies, internal crystal structures and associated impurities (Figs. 9a, b, 15b). This replacement apparently took place early within a few tens of centimeters of burial depth. According to Schreiber and Walker (1992) and Hovorka (1992), halite replacement of gypsum is linked to temperature variations and associated changes in the solubility of both minerals following chemical changes in the brine composition, in our case probably related to salinity changes of the water in the repetitive, early-diagenetic, dissolution–precipitation cycles.

Nodular anhydrite replaces pre-existing halite crystals (Fig. 8h) and locates at the base and on top of halite beds (*E2* facies; Fig. 7a). The $^{87}Sr/^{86}Sr$ and the $\delta^{34}S_{V\text{-}CDT}$ signatures of halite and anhydrite are quite similar, pointing to an early process preventing a strong isotopic fractionation.

Pyrite is found as framboid growths (spherical aggregates of micron-sized pyrite crystals; Love and Amstutz 1966; Sweeney and Kaplan 1973). Framboid pyrite is associated with plant debris (Figs. 6f, 9c). According to Berner (1970), it results from the reaction of sulfide (produced via bacterial sulfate reduction; BSR) with either Fe^{3+} (in sediments) or Fe^{2+} produced by bacterial Fe^{3+} reduction (Lovley 1991). Thus, the presence of pyrite suggests that BSR processes occurred during early diagenesis in the ISU sediments.

5.3.3 Intermediate- to late-diagenetic stages

Authigenic silica, equigranular quartz (megaquartz), and fibrous quartz (chalcedony and lutecite), replaces pre-existing evaporites (i.e. secondary, mosaic halite, and anhydrite crystals). The sequence of silica replacement is from megaquartz (Fig. 9d, e), to chalcedony (Fig. 9f), and to lutecite (Fig. 9g–i). All these quartz varieties have been reported as a testimony of vanished evaporites (Folk and Pittman 1971;

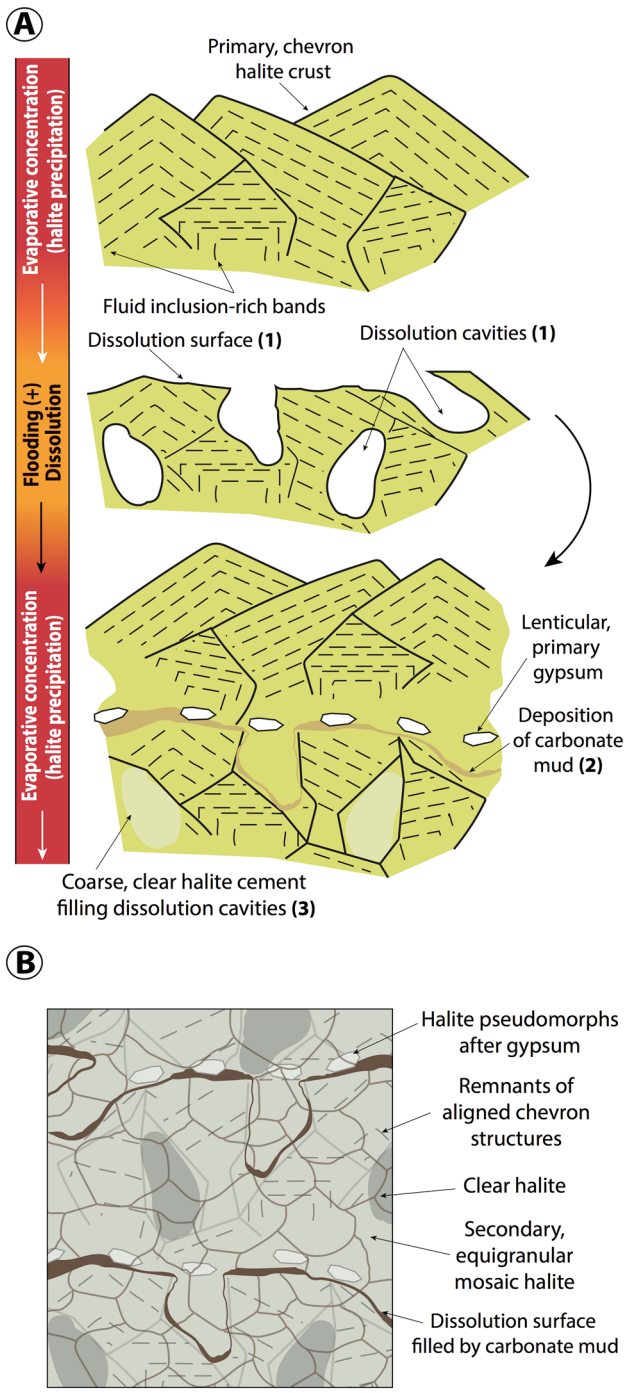

Fig. 15 **a** Simplified diagram illustrating syn-depositional overprints on primary, chevron-type halite (after Shearman 1970, modified). The textural evolution of halite crust shows: (1) dissolution on top of primary halite, (2) deposition of mud, and (3) precipitation of halite cement in the dissolution cavities. **b** Simplified diagram illustrating re-crystallization of halite and formation of secondary, mosaic-halite driven by repetitive dissolution/precipitation (evaporative concentration) cycles

Friedman and Shukla 1980). According to Folk and Pittman (1971) and Arbey (1980) silica-crystal size and morphology are controlled by the sulfate content within the diagenetic environment. Megaquartz forms in non-sulfated (or poorly sulfated) diagenetic environments. On the contrary, chalcedony and lutecite crystallize in sulfated diagenetic environments. A low pH promotes chalcedony formation, while a high pH favors lutecite crystallization (Arbey 1980).

According to Tucker (1976), Geeslin and Chafetz (1982), and Maliva (1987), anhydrite replacement by quartz is an early diagenetic process. However, silicification of anhydrite nodules has been related to burial diagenesis when hydrocarbon inclusions are found inside the megaquartz (Ulmer-Scholle et al. 1993), and hydrothermalism cannot be ruled out to explain the crystallization of lutecite (Arbey 1980). According to García-Veigas et al. (2013), halite precipitation in the UHU of the Chimeneas Halite is associated with significant, underground water inputs, including $CaCl_2$-rich, sulfate-depleted, hydrothermal waters. Percolating brines from the UHU with such as fluid chemistry could explain the formation of megaquartz in the underlying ISU.

The diagenetic conditions in the ISU appear to have changed from non-sulfated (or poorly sulfated), as confirmed by the anhydrite replacement to megaquartz, to more sulfated conditions, as attested to by the crystallization of chalcedony and lutecite. In this respect, it is worth noting that the Chimeneas Halite Unit is capped by a thick gypsum sequence (Fig. 1) reflecting a major shift in brine composition to sulfate-rich fluids, and presumably, in the same way, in the fluids percolating through the underlying deposits (i.e. the ISU deposits).

Celestine occurs as a late-diagenetic replacement of lutecite after mosaic halite (Fig. 9i). Celestine occurrences are commonly interpreted as result of the diagenetic interaction of Ca-sulfates with Sr^{2+}-rich groundwater (e.g. Warren 2016). The dissolution of gypsum or anhydrite supplies the SO_4, which combined with Sr^{2+}-rich waters lead to the precipitation of celestine. The large celestine orebodies (Montevive and Escúzar ore deposits; Martín et al. 1984; García-Veigas et al. 2015) of the Granada Basin (Fig. 1) formed by early diagenetic replacement of gypsified stromatolites (García-Veigas et al. 2015). According to García-Veigas et al. (2015), dissolved gypsum was the main sulfate source, while marine waters and diagenetic–hydrothermal $CaCl_2$ brines were the main strontium sources. The small celestine crystals found at ISU (Fig. 10i) could be the result of recycling by underground waters of some of the previously formed celestine.

5.4 Brine parenthood

Basin architecture, tectonic evolution and climate of the Granada Basin in the latest Tortonian were appropriate to

establish a basin-wide, evaporite depositional environment (Martín et al. 1984) (Fig. 3). In the Granada Basin salt succession, three thick halite-bearing units were identified: the 'Lower Halite Unit' (LHU), the 'Intermediate Sandstone Unit' (ISU), and the 'Upper Halite Unit' (UHU). Geochemical markers (brine inclusion composition, bromine content, and isotope data) indicate a marine origin for the LHU, with a growing influence of non-marine input higher in the sequence. The environment of deposition for the LHU was envisaged as a salt-concentrated, marine lagoon (García-Veigas et al. 2013). In the ISU and UHU, the non-marine influences became progressively more significant, with geochemical markers suggesting recycling of previously formed halite and also contribution from hydrothermal waters. The UHU environment of deposition was that of a continental salt-pan, clearly disconnected from the sea (García-Veigas et al. 2013).

The ISU marks the transition from a marine to a continental setting for the precipitation of the salt in the Granada Basin. As stated above, the deposition environment for the ISU was that of a coastal lake, isolated from the open sea by a sand barrier and subjected to strong salinity fluctuations. In the ISU evaporitic deposits, $^{87}Sr/^{86}Sr$ isotopic values (Fig. 11) are slightly lower than those of the Tortonian seawater (Hodell et al. 1991). The strontium ($^{87}Sr/^{86}Sr$) and sulfur ($\delta^{34}S$) isotope compositions are midway between the marine Miocene (Paytan et al. 1998; Hodell et al. 1991) and the Triassic basement (evaporite and dolomite) values (Gorzawski et al. 1989; García-Veigas et al. 2013; Ortí et al. 2014b) (Fig. 11). All this suggests a mixed origin, between non-marine (underground/hydrothermal) and marine waters, for the parenthood brines.

ISU sulfate isotope values ($\delta^{34}S$ and $\delta^{18}O$) are very close to those found by Rouchy and Pierre (1979) for the Granada Basin Tortonian gypsum (Figs. 10, 11). The sulfur and oxygen signatures are also similar to some of those recorded in continental evaporites from the Calatayud and Tajo Basins (Utrilla et al. 1992; Fig. 10). According to these authors, such signatures resulted from the remobilization of marine Triassic evaporites. Sulfur and oxygen enrichment in the ISU evaporites compared to Triassic evaporites (Figs. 10, 11) could be the result of the combined effects of bacterial sulfate reduction (BSR), fractional crystallization, and strong evaporation. According to Antler et al. (2013) a positive covariance between oxygen and sulfur isotope compositions points to BSR. During BSR the sulfur and oxygen isotope values of the residual, dissolved sulfate, and sulfide increases and decreases, respectively (Seal et al. 2000). Our data are in line with such considerations and suggest strong BSR in an anoxic environment during ISU deposition.

Additional contribution of $CaCl_2$-rich hydrothermal fluids to the ISU brines, as suggested by García-Veigas et al. (2013), cannot be disregarded. Diagenetic-hydrothermal, $CaCl_2$-rich brines have been proposed to explain the 'selected removal' of sulfate ions in many evaporite basins (Ayora et al. 1994b, 2001; Cendón et al. 2008; García-Veigas et al. 2009; Lowenstein and Risacher 2009; García-Veigas et al. 2013; 2015), favoring the precipitation of halite instead of gypsum. $CaCl_2$-rich brines form by diagenetic interactions between rock/sediment and heated groundwaters (e.g. Hardie 1990; Lowenstein and Risacher 2009). These brines can reach the subsurface by convective- or topographically driven circulation (Hardie 1990), associated mainly with volcanism and faulting.

The eastern Betic Cordillera, as revealed by many authors, recorded the synchronous interaction of tectonic, volcanic, hydrothermal and evaporitic processes in the course of the late Miocene (e.g. Benito et al. 1999; Dinarès-Turell et al. 1999; Kuiper et al. 2006; Playà and Gimeno 2006). However, such as evidence does not exist, particularly concerning volcanism, in the case of the Granada Basin. Basinal brines migrating upwards along faults in a tectonically active basin seem to be the most plausible scenario for the Granada Basin. As stated above, major fault systems in the Granada Basin have NW–SE and E–W orientations, such as the 'Cádiz-Alicante fault' (Sanz de Galdeano 2008), delineating its northern margin (Fig. 2), and the 'La Malahá fault' (Rosino 2008), limiting the salt depocenter (Fig. 3). The reactivation of such faults at the end of the Miocene (Montenat et al. 1990; Sanz de Galdeano 1990; Rodríguez-Fernández and Sanz de Galdeano 2006) promoted convective flow of groundwaters in areas of the basin with elevated heat flows and could also have facilitated the circulation of hydrothermal fluids (i.e. $CaCl_2$-rich brines) presumably coming from deep underground (Fig. 16).

The Lorca basin is a comparable example to that of the Granada basin (García-Veigas et al. 2013). This basin is also limited by the Cádiz-Alicante fault (Sanz de Galdeano 1990, Fig. 2a), and its Upper Miocene record also encompasses a marine, an evaporitic, and a continental succession, from bottom to top (Geel 1976; Krijgsman et al. 2000; Taberner

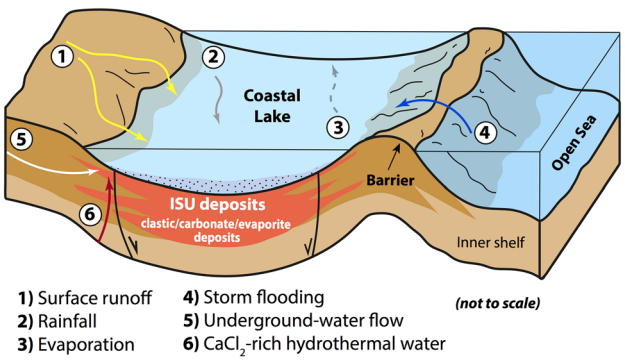

Fig. 16 Hydrology model during the deposition of the ISU in the Granada Basin

et al. 2000). The marine sequence culminated with the deposition of a 'Gypsum Member', which also includes a thick (> 200 m) halite deposit (García-Veigas 1993; Ayora et al. 1994b; Taberner et al. 2000). Based on geochemical evidence, García-Veigas (1993) and Ayora et al. (1994b) differentiated within the Halite Unit a marine Lower Part and a continental Upper Part. According to these authors, upper halite deposition took place under non-marine conditions and resulted from the input into the basin of saline underground waters recycling older evaporites (i.e. Keuper evaporites) and hydrothermal, $CaCl_2$-rich waters coming from deep underground through major faults. Sedimentological interpretations combined with geochemical analyses in both Granada and Lorca basins point to a similar evolution from marine to non-marine conditions. Recent biostratigraphic studies (Corbí et al. 2012), however, suggest that the evaporites of the Granada Basin could be younger than those from the Lorca basin.

6 Conclusions

The Granada Basin contains a thick salt sequence (Chimeneas Halite) formed at the time the basin desiccated during the latest Tortonian. The salt succession comprises three halite-bearing units: the 'Lower Halite Unit' (LHU), the 'Intermediate Sandstone Unit' (ISU), and the 'Upper Halite Unit' (UHU). Detailed sedimentological and petrographical core observations, combined with isotopic analysis ($\delta^{34}S$ and $\delta^{18}O$ in sulfates and $^{87}Sr/^{86}Sr$ in sulfate and halite samples), of the ISU yield the following conclusions:

In the ISU deposits, six major facies-types are distinguished: bioclastic sandstones (*C1*); bioclastic siltstones (*C2*); carbonate mudstones (*CB1*); carbonate-anhydrite interbeds (*CE1*); nodular-anhydrite beds (*E1*) and banded halite (*E2*). The bioclastic sandstones (*C1* facies) are interpreted as marine sediments redeposited, as storm layers, inside a coastal lake. The bioclastic siltstones (*C2* facies) are considered to be suspension deposits, of marine origin, introduced as well in the lake by storms. Carbonate mudstones (*CB1* facies) are thought to represent inorganic, lacustrine chemical precipitates. Anhydrite laminae (in *CE1* facies) are interpreted to have formed at the bottom of the lake by syn-sedimentary replacement of micro-selenite-gypsum. Nodular-anhydrite (*E1* facies) seems to have developed within carbonate mud by the replacement of gypsum, and primary-halite crystals (in *E2* facies) are considered to be in situ growths, deposited sub-aqueously at the bottom of the lake.

The environment of deposition for the ISU was that of a coastal lake, isolated from the open sea by a sand barrier. We propose the precise boundary of the onset of marine to non-marine conditions in the Granada Basin to be placed during the ISU deposition. Three main stages are recognized in the evolution of the lake. At stage 1, syn-depositional anhydrite nodules formed close to the surface in a very shallow lacustrine environment. At stage 2, frequent marine flooding storm events resulted in significant bioclastic, sandy sedimentation in a presumably deeper lake. At stage 3, a shallower, perennial saline lake was established and major evaporite deposition (anhydrite after micro-selenite gypsum, and primary chevron halite) took place. Dissolution surfaces developed on top of halite layers (*E2* facies) after flooding events. Clear-halite, void-filling cement precipitated syn-depositionally inside primary-halite, dissolution cavities.

Early diagenesis is shown by: halite re-crystallization of pre-existing halite (depositional halite and syn-depositional halite cement), as a result of repetitive dissolution–precipitation cycles; gypsum replacement by halite, and halite replacement by nodular anhydrite. The presence of framboid pyrite associated with plant debris suggests BSR taking place during early diagenesis in the ISU sediments.

Intermediate- to late-diagenetic processes are silica (megaquartz, chalcedony, and lutecite) replacement of halite and anhydrite, and celestine formation. Megaquartz formed within a poorly sulfated, diagenetic environment. Percolating brines, at the time of deposition of the UHU, seem to be the most likely fluids responsible for the existence of megaquartz in the underlying ISU. Chalcedony and lutecite crystallized sometime later, presumably during deposition of the gypsum sequence occurring on top of the Chimeneas Halite Unit. This implied a major change to a sulfate-rich brine and, in a similar way, in the chemistry of the fluids percolating through the underlying ISU deposits. Celestine found at ISU replacing lutecite could be the result of the interaction with Sr-rich underground waters dissolving some of the previously formed celestine (Montevive/Escúzar Celestine ore deposits).

Strontium and sulfur isotope compositions are midway between the Miocene marine signature and the Triassic basement, evaporite and dolomite signatures. This suggests a mixed origin, between non-marine (underground) and marine waters, for the parenthood brines, during evaporite deposition. Additional contribution of hydrothermal, $CaCl_2$-rich basinal brines, migrating upwards along faults, cannot be ruled out.

Acknowledgements This work is part of the 'Study MFT08.003' (IFP Énergies Nouvelles, France). The initial part of this work was carried out at IFP Énergies Nouvelles laboratories in Rueil-Malmaison (France), during an internship stay of the senior author (ALQ) sponsored by IFP. JMM work was funded by the project 'Productores de carbonato en plataformas carbonatadas neógenas de la Cordillera Bética. Factores que controlan la composición y la resedimentación' (CGL2013-47236-P) (2014-18) (Ministerio de Economía y Competitividad, Spain and Fondo Europeo de Desarrollo Regional FEDER). Thanks are given to Dr. Javier García-Veigas (University of Barcelona) for the critical reading of an earlier version of this paper and for helping

with the isotopic analysis carried out at the CCiT-UB (*Centres Científics i Tecnològics, Universitat de Barcelona*), and to SUERC (*Scottish Universities Environmental Research Centre*) for the strontium isotopic analysis. We would also thank Dr. Ángel Puga-Bernabéu and Dr. Julio Aguirre (University of Granada) for their helpful contribution to this work. The authors would like to express their sincere thanks to the Editorial Board and anonymous reviewer for their suggestions to improve the paper. We thank David Nesbit for the correction of the English text.

References

Aldaya, F., Vera, J. A., & Fontboté, J. M. (1980). Memoria Mapa Geológico de la Hoja nº 83 (Granada-Málaga). Mapa Geológico de España Escala 1:200.000. Segunda Serie (MAGNA), Primera edición. Instituto Geológico y Minero de España (Madrid).

Antler, G., Turchyn, A. V., Rennie, V., Herut, B., & Sivan, O. (2013). Coupled sulfur and oxygen isotope insight into bacterial sulfate reduction in the natural environment. *Geochimica et Cosmochimica, 118,* 98–117.

Arbey, F. (1980). Les formes de la silica et l'identification des évaporites dans les formations silicifies; in Les évaporites, méchanismes, diagenese et applications: Centre de la Recherche, Exploration et Production Elf-Aquitaine. *Bulletin, 4,* 309–365.

Aref, M. A. M., Attia, O. E. A., & Wali, A. M. A. (1997). Facies and depositional environment of the Holocene evaporites in the Ras Shukeir area, Gulf of Suez, Egypt. *Sedimentary Geology, 110,* 123–145.

Ayora, C., Cendón, D. I., Taberner, C., & Pueyo, J. J. (2001). Brine-mineral reactions in evaporite basins: Implications for the composition of ancient oceans. *Geology, 29,* 251–254.

Ayora, C., García-Veigas, J., & Pueyo, J. J. (1994a). The chemical and hydrological evolution of an ancient potash-forming evaporite basin as constrained by mineral sequence, fluid inclusion composition and numerical simulation. *Geochimica et Cosmochimica Acta, 58,* 3379–3394.

Ayora, C., García-Veigas, J., & Pueyo, J. J. (1994b). X-ray microanalysis of fluid inclusions and its application to the geochemical modeling of evaporite basins. *Geochimica et Cosmochimica Acta, 58,* 43–55.

Ayora, C., Taberner, C., Pierre, C., & Pueyo, J. J. (1995). Modeling the sulfur and oxygen isotopic composition of sulfates through a halite-potash sequence: Implications for the hydrological evolution of the Upper Eocene Southpyrenean basin. *Geochimica et Cosmochimica Acta, 59,* 1799–1808.

Benison, K. C., & Goldstein, R. H. (2001). Evaporites and siliciclastics of the Permian Nippewalla Group of Kansas, USA: A case for non-marine deposition in saline lakes and saline pans. *Sedimentology, 48,* 165–188.

Benito, R., López-Ruiz, J., Cebriá, J. M., Hertogen, J., Doblas, M., Oyarzun, R., et al. (1999). Sr and O isotope constraints on source and crustal contamination in the high-K calc-alkaline and shoshonitic neogene volcanic rocks of SE Spain. *Lithos, 46,* 773–802.

Berner, R. A. (1970). Sedimentary pyrite formation. *American Journal of Sciences, 268,* 1–23.

Betzler, C., Brachert, T., Braga, J. C., & Martín, J. M. (1997). Nearshore, temperate, carbonate depositional systems (lower Tortonian, Agua Aargau Basin, southern Spain): Implications for carbonate sequence stratigraphy. *Sedimentary Geology, 113,* 27–53.

Birnbaum, S. J., & Coleman, N. (1979). Source of sulphur in the Ebro basin (northern Spain). Tertiary nonmarine evaporite deposits as evidenced by sulphur isotopes. *Chemical Geology, 25,* 163–168.

Braga, J. C., Martín, J. M., & Alcalá, B. (1990). Coral reefs in coarse-terrigenous sedimentary environments (Upper Tortonian, Granada Basin, southern Spain). *Sedimentary Geology, 66,* 135–150.

Braga, J. C., Martín, J. M., Betzler, C., & Aguirre, J. (2006). Models of temperate carbonate deposition in Neogene basins in SE Spain: A synthesis. In M. Pedley & G. Carannante (Eds.), *Cool-water carbonates: Depositional systems and palaeoenvironmental control* (Vol. 255, pp. 121–135). London: Geological Society, Special Publications.

Braga, J. C., Martín, J. M., & Quesada, C. (2003). Patterns and average rates of late Neogene–Recent uplift of the Betic Cordillera, SE Spain. *Geomorphology, 50,* 3–26.

Casas, E., & Lowenstein, T. K. (1989). Diagenesis of saline pan halite: Comparison of petrographic features of modern, quaternary and permian halites. *Journal of Sedimentary Petrology, 59*(5), 724–739.

Cendón, D. I., Ayora, C., Pueyo, J. J., Taberner, C., & Blanc-Valleron, M. M. (2008). The chemical and hydrological evolution of the Mulhouse potash basin (France). Are "marine" ancient evaporites always representative of synchronous seawater chemistry? *Chemical Geology, 252,* 109–124.

Claypool, G. E., Holser, W. T., Kaplan, I. R., Sakai, H., & Zak, I. (1980). The age curves of sulfur and oxygen isotopes in marine sulfate and their mutual interpretation. *Chemical Geology, 28,* 199–260.

Corbí, H., Lancis, C., García-García, F., Pina, J. A., Soria, J. M., Tent-Manclús, J. E., et al. (2012). Updating the marine biostratigraphy of the Granada Basin (central Betic Cordillera). Insight for the Late Miocene palaeogeographic evolution of the Atlantic–Mediterraneas seaway. *Geobios, 45,* 249–263.

Dabrio, C. J., & Martín, J. M. (1981). Yesos diagenéticos en la Depresión de Granada. Boletín de la Real Sociedad Española de Historia Natural. *Sección Geología, 79,* 215–223.

Dabrio, C. J., Martín, J. M., & Megias, A. (1982). Signification sédimentaire des évaporites de la depression de Granade (Espagne). *Bulletin de la Societe Geologique de France, 24,* 705–710.

Dewey, J. F., Helman, M. L., Turco, E., Hutton, D. H. W., & Knott, T. S. D. (1989). Kinematics of the western Mediterranean. In M. P. Coward, D. Dietrich, & R. G. Park (Eds.), *Alpine tectonics* (Vol. 45, pp. 265–283). London: Geological Society, Special Publication.

Dinarès-Turell, J., Ortí, F., Playà, E., & Rosell, L. (1999). Palaeomagnetic chronology of the evaporitic sedimentation in the Neogene Fortuna Basin (SE Spain): Early restriction preceding the Messinian Salinity Crisis. *Palaeogeography, Palaeoclimatology, Palaeoecology, 154,* 161–178.

Evans, G. (1995). The Arabian Gulf: A modern carbonate–evaporite factory, a review. *Cuadernos de Geología Ibérica, 19,* 61–96.

Fernández, J., Soria, J., & Viseras, C. (1996). Stratigraphic architecture of the Neogene basins in the central sector of the Betic Cordillera (Spain); tectonic control and base level changes. In P. F. Friend & C. J. Dabrio (Eds.), *Tertiary Basins of Spain: The stratigraphic record of crustal kinematics* (pp. 353–365). Cambridge: Cambridge University Press.

Folk, R. L., & Pittman, J. S. (1971). Length-slow chalcedony; a new testament for vanished evaporites. *Journal of Sedimentary Petrology, 41,* 1045–1058.

Friedman, G. M., & Shukla, V. (1980). Significance of authigenic quartz euhedra after sulfates; example from the Lockport Formation (Middle Silurian) of New York. *Journal of Sedimentary Geology, 50,* 1299–1304.

García-Alix, A., Minwer-Barakat, R., Martín, J. M., Martín-Suarez, E., & Freudenthal, M. (2008). Biostratigraphy and sedimentary evolution of Late Miocene and Pliocene continental deposits of the Granada Basin (southern Spain). *Lethaia, 41,* 431–446.

García-Veigas, J. (1993). *Geoquímica de inclusiones fluidas en formaciones salinas. Microanálisis cryo-SEM-EDS*. Mem. Tesis Doctoral, Universidad Barcelona.

García-Veigas, J., Cendón, D. I., Rosell, L., Ortí, F., Torres Ruiz, J., Martín, J. M., et al. (2013). Salt deposition and brine evolution in the Granada Basin (Late Tortonian, SE Spain). *Palaeogeography, Palaeoclimatology, Palaeoecology, 369,* 452–465.

García-Veigas, J., Rosell, L., Cendón, D. I., Gibert, L., Martín, J. M., Torres Ruiz, J., et al. (2015). Large celestine orebodies formed by early-diagenetic replacement of gypsified stromatolites (upper Miocene, Montevive-Escúzar deposits, Granada basin, Spain). *Ore Geology Reviews, 64,* 187–199.

García-Veigas, J., Rosell, L., Zak, I., Playà, E., Ayora, C., & Starinsky, A. (2009). Evidence of potash salt formation in the Pliocene Sedom Lagoon (Dead Sea Rift, Israel). *Chemical Geology, 265,* 499–511.

Geel, T. (1976). Messinian gypsiferous deposits of the Lorca basin (province of Murcia, SE Spain). *Memorie della Società Geologica Italiana, 16,* 369–385.

Geeslin, J. H., & Chafetz, H. S. (1982). Ordovician Aleman ribbon cherts: An example of silicification prior to carbonate lithification. *Journal of Sedimentary Petrology, 52,* 1283–1293.

Gorzawski, H., Fontboté, L., Sureau, F., & Calvez, J. Y. (1989). Strontium isotope trends during diagenesis in ore-bearing carbonate basins. *Geologische Rundshau, 78*(1), 268–290.

Handford, R. C. (1982). Sedimentology and evaporite genesis in a Holocene continental-sabkha playa basin—Bristol Dry Lake, California. *Sedimentology, 29,* 239–253.

Hardie, L. A. (1984). Evaporites: Marine or non-marine? *American Journal of Science, 284,* 193–240.

Hardie, L. A. (1990). The roles of rifting and hydrothermal $CaCl_2$ brines in the origin of potash evaporites: An hypothesis. *American Journal of Science, 290,* 43–106.

Hodell, D. A., Mueller, P. A., & Garrido, J. (1991). Variations in the strontium isotopic composition of seawater during the Neogene. *Geology, 19,* 24–27.

Holdoway, K. A. (1978). *Deposition of evaporites and red beds of the Nippewalla Group, Permian, western Kansas* (Vol. 215). Kansas Geological Survey, Bulletin.

Holliday, D. W. (1973). Early diagenesis in nodular anhydrite rocks. *Transactions of the Institute of Mining and Metallurgy, 82,* 81–84.

Holser, W. T. (1979). Mineralogy of evaporites. In R. G. Burns (Ed.), *Marine minerals* (Vol. 6, pp. 124–150). Mineralogical Society of America. Short Course Notes.

Holser, W. T., & Kaplan, I. R. (1966). Isotope geochemistry of sedimentary sulfates. *Chemical Geology, 1,* 93–135.

Hovorka, S. D. (1992). Halite pseudomorphs after gypsum in bedded anhydrite ± clue to gypsum–anhydrite relationships. *Journal of Sedimentary Petrology, 62,* 1098–1111.

Jabaloy, A., Galindo-Zaldivar, J., & González Lodeiro, F. (2002). Palaeostress evolution of the Iberian Peninsula (Late Carboniferous to present). *Tectonophysics, 357,* 159–186.

Kendall, A. C., & Harwood, G. M. (1996). Marine evaporites: Arid shorelines and basins. In H. G. Reading (Ed.), *Sedimentary environments: Processes, facies and stratigraphy* (pp. 281–324). Londres: Blackwell Science.

Kirkham, A. (1997). Shoreline evolution, aeolian deflation and anhydrite distribution of the Holocene, Abu Dhabi. *GeoArabia, 2,* 403–416.

Krijgsman, W., Garcés, M., Agustí, J., Raffi, I., Taberner, C., & Zachariasse, W. J. (2000). The ''Tortonian Salinity Crisis'' of the eastern Betics (Spain). *Earth and Planetary Science Letters, 181,* 497–511.

Krijgsman, W., Leewis, M. E., Garcés, M., Kouwenhoven, T. J., Kluiper, K. F., & Sierro, F. J. (2006). Tectonic control for evaporite formation in the Eastern Betics (Tortonian; Spain). *Sedimentary Geology, 188–189,* 155–170.

Kuiper, K. F., Krijgsman, W., Garcés, M., & Wijbrans, J. R. (2006). Revised isotopic ($^{40}Ar/^{39}Ar$) age for the lamproite volcano of Cabezos Negros, Fortuna Basin (Eastern Betics, SE Spain). *Palaeogeography, Palaeoclimatology, Palaeoecology, 238,* 53–63.

López-Quirós, A., Barbier, M., Martín, J. M., Puga-Bernabéu, Á., & Guichet, X. (2016). Diagenetic evolution of Tortonian temperate carbonates close to evaporites in the Granada Basin (SE Spain). *Sedimentary Geology, 335,* 180–196.

Lotze, F. (1957). *Steinsalz und Kalisalze, I* (p. 465). Berlin: Gebrüder Borntträeger.

Love, L. G., & Amstutz, G. C. (1966). Review of microscopic pyrite from the Devonian Chattanooga Shale and Rammelsberg Banderz. *Fortschr Mineralium, 43,* 272–309.

Lovley, D. R. (1991). Dissimilatory Fe(III) and Mn(IV) reduction. *Microbiology Reviews, 55,* 259–287.

Lowenstein, T. K., & Hardie, L. A. (1985). Criteria for the recognition of salt-pan evaporites. *Sedimentology, 32,* 627–644.

Lowenstein, T., & Risacher, F. (2009). Closed basin brine evolution and the influence of Ca–Cl inflow waters: Death Valley and Bristol Dry lake, California, Qaidam Basin, China, and Salar de Atacama, Chile. *Aquatic Geochemistry, 17,* 71–94.

Lowenstein, T. K., & Spencer, R. J. (1990). Syndepositional origin of potash evaporites: Petrographic and fluid inclusions evidence. *American Journal of Science, 290,* 1–42.

Maiklem, W. R., Bebout, R. P., & Glaister, R. P. (1969). Classification of anhydrite: A practical approach. *Bulletin of Canadian Petroleum Geology, 17*(2), 194–233.

Maliva, R. G. (1987). Quartz geodes; early diagenetic silicified anhydrite nodules related to dolomitization. *Journal of Sedimentary Petrology, 57,* 1054–1059.

Martín, J. M., & Braga, J. C. (1997). Sierra Nevada: Historia del levantamiento de un relieve deducida de las unidades conglomeráticas de su borde. In J. P. Calvo & J. Morales (Eds.), *Avances en el conocimiento del Terciario Ibérico*. *Grupo Español del Terciario* (pp. 117–120). Madrid: Universidad Complutense de Madrid-Museo Nacional de Ciencias Naturales.

Martín, J. M., Braga, J. C., Betzler, C., & Brachert, T. (1996). Sedimentary model and high-frequency cyclicity in a Mediterranean, shallow-shelf, temperate-carbonate environment (uppermost Miocene, Agua Amarga Basin, southern Spain). *Sedimentology, 43,* 263–277.

Martín, J. M., Braga, J. C., Sánchez-Almazo, I. M., & Aguirre, J. (2010). Temperate and tropical carbonate-sedimentation episodes in the Neogene Betic basin (southern Spain) linked to climatic oscillations and changes in Atlantic–Mediterranean connections: Constraints from isotopic data. *International Association of Sedimentologist, Special Publication, 42,* 49–70.

Martín, J. M., Ortega-Huertas, M., & Torres-Ruiz, J. (1984). Genesis and evolution of strontium deposits of the Granada Basin (southeastern Spain): Evidence of diagenetic replacement of a stromatolite belt. *Sedimentary Geology, 39,* 281–298.

Martín, J. M., Puga-Bernabéu, A., Aguirre, J., & Braga, J. C. (2014). Miocene Atlantic–Mediterranean seaways in the Betic Codillera (southern Spain). *Revista de la Sociedad Geológica de España, 27*(1), 175–186.

Middleton, G. V. (1973). Johannes Walther's Law of the correlation of facies. *Geological Society of America Bulletin, 84,* 970–988.

Montenat, C., Ott d'Estevou, P., & Coppier, G. (1990). Les bassins néogènes entre Alicante et Cartagena. In Ch. Montenat (Ed.), *Les basins néogènes du domaine bétique oriental (Espagne)* (pp. 313–368). Paris: Doc. Trav. IGAL 12–13.

Morales, J., Vidal, F., de Miguel, D., Aguacil, G., Posadas, A. M., Ibáñez, J. M., et al. (1990). Basement structure of the Granada

Basin, Betic Cordilleras, southern Spain. *Tectonophysics, 177,* 337–348.

Nielsen, H. (1972). Sulphur isotopes and the formation of evaporite deposits. In G. Richter Bernburg (Ed.), *Geology of saline deposits* (Vol. 7, pp. 91–102). Paris: UNESCO.

Ortí, F., Pérez-López, A., García-Veigas, J., Rosell, L., Cendón, D. I., & Pérez-Valera, F. (2014a). Sulfate isotope compositions ($\delta^{34}S$, $\delta^{18}O$) and strontium isotopic ratios ($^{87}Sr/^{86}Sr$) of Triassic evaporites in the Betic Cordillera (SE Spain). *Revista de la Sociedad Geológica de España, 27*(1), 79–89.

Ortí, F., Rosell, L., Gibert, L., Moragas, M., Playà, E., Inglés, M., et al. (2014b). Evaporite sedimentation in a tectonically active basin: The lacustrine Las Minas Gypsum unit (Late Tortonian, SE Spain). *Sedimentary Geology, 311,* 17–42.

Paytan, A., Kastner, M., Campbell, D., & Thiemens, M. H. (1998). Sulfur isotopic composition of Cenozoic seawater sulfate. *Science, 282,* 1459–1462.

Pierre, C. (1985). Isotopic evidence for the dynamic redox cycle of dissolved sulphur compounds between free and interstitial solutions in marine salt pans. *Chemical Geology, 53,* 191–196.

Pierre, C. (1989). Sedimentation and diagenesis in restricted marine basins. In P. Fritz & J. Ch. Fontes (Eds.), *Handbook of environmental isotope geochemistry* (Vol. 3, pp. 257–315). The marine environment. Amsterdan: Elsevier.

Playà, E., & Gimeno, D. (2006). Evaporite deposition and coeval volcanism in the Fortuna Basin (Neogene, Murcia, Spain). *Sedimentary Geology, 188–189,* 205–218.

Puga-Bernabéu, A., Martín, J. M., & Braga, J. C. (2007). Tsunami-related deposits in temperate carbonate ramps, Sorbas basin, southern Spain. *Sedimentary Geology, 199,* 107–127.

Puga-Bernabéu, Á., Martín, J. M., & Braga, J. C. (2008). Sedimentary processes in a submarine canyon excavated into a temperate-carbonate ramp (Granada basin, S. Spain). *Sedimentology, 55,* 1449–1466.

Rodríguez-Fernández, J., & Sanz de Galdeano, C. (2006). Late orogenic intramontane basin development: The Granada basin, Betics (southern Spain). *Basin Research, 18,* 85–102.

Rosino, J. (2008). Modelo hidrogeológico conceptual de las aguas termo- minerales de la Depresión de Granada. En: J. A. López-Geta et al. (Editores), *Agua y Cultura. VII Simposio sobre el Agua en Andalucía (SIAGA-08), IGME*, pp. 1107–1118.

Rouchy, J. M., & Pierre, C. (1979). Données sédimentologiques et isotopiques sur gypses des séries évaporitiques messiniennes d'Espagne méridionale et de Chypre. *Revue de Géologie Dynamique et de Géographie Physique, 21,* 267–280.

Sanz de Galdeano, C. (1990). Geologic evolution of the Betic Cordilleras in the western Mediterranean, Miocene to the present. *Tectonophysics, 172,* 107–119.

Sanz de Galdeano, C. (2008). The Cádiz-Alicante fault: An important discontinuity in the Betic Cordillera. *Revista de la Sociedad Geológica de España, 21,* 49–58.

Sanz de Galdeano, C., & Alfaro, P. (2004). Tectonic significance of the present relief of the Betic Cordillera. *Geomorphology, 63,* 178–190.

Sanz de Galdeano, C., & Vera, J. A. (1991). Una propuesta de clasificación de cuencas neógenas béticas. *Acta Geológica Hispánica, 26,* 205–277.

Sanz de Galdeano, C., & Vera, J. A. (1992). Stratigraphic record and palaeogeographical context of the Neogene basins in the Betic Cordillera, Spain. *Basin Research, 4,* 21–36.

Sarg, J. F. (2001). The sequence stratigraphy, sedimentology, and economic importance of evaporite-carbonate transitions: A review. *Sedimentary Geology, 140,* 9–42.

Savostin, L. A., Sibuet, J. C., Zonenshain, L. P., Le Pichon, X., & Roulet, M. J. (1986). Kinematic evolution of the Tethys belt from the Atlantic Ocean to the Pamirs since the Triassic. *Tectonophysics, 123,* 1–35.

Schléder, Z., & Urai, J. L. (2005). Microstructural evolution of deformation-modified primary halite from the Middle Triassic Röt Formation at Hengelo, The Netherlands. *International Journal of Earth Sciences, 94,* 941–955.

Schreiber, B. C., & El Tabakh, M. (2000). Deposition and early alteration of evaporites. *Sedimentology, 47*(1), 215–238.

Schreiber, B. C., Friedman, G. M., Decima, A., & Schreiber, E. (1976). The depositional environments of the Upper Miocene (Messinian) evaporite deposits of the Sicilian Basin. *Sedimentology, 23,* 729–760.

Schreiber, B. C., & Kinsman, D. J. J. (1975). New observations on the Pleistocene evaporites of Montallegro, Sicily and a modern analog. *Journal of Sedimentary Petrology, 45,* 469–479.

Schreiber, B. C., & Walker, D. (1992). Halite pseudomorphs after gypsum: A suggested mechanism. *Journal of Sedimentary Petrology, 62,* 61–70.

Seal, R. R., Alpers, C. N., & Rye, R. O. (2000). Stable isotope systematics of sulfate minerals. *Reviews in Mineralogy and Geochemistry, 40,* 541–602.

Shearman, D. J. (1970). Recent halite rock, Baja California, Mexico. *Transactions of the Institution of Mining and Metallurgy, 79B,* 155–162.

Shearman, J., & Fuller, J. G. (1969). Anhydrite diagenesis, calcitization, and organic laminites. Winnipegosis Formation, Middle Devonian, Saskatchewan. *Bulletin of Canadian petroleum Geology, 17,* 496–525.

Smith, D. B. (1971). Possible displacive halite in the Permian Upper Evaporite Group of northeast Yorkshire. *Sedimentology, 17,* 221–232.

Strakhov, N. M. (1970). *Principles of lithogenesis* (Vol. 3). Edinburgh: Oliver & Boyd.

Strohmenger, C. J., Shebl, H., Al-Mansoori, A., Al-Mehsin, K., Al-Jeelani, O., Al-Hosani, I., et al. (2011). Facies stacking patterns in a modern arid environment: A case study of the Abu Dhabi sabkha in the vicinity of Al-Qanatir Island, United Arab Emirates. In A. S. Alsharhan & C. G. S. C. Kendall (Eds), *Quaternary carbonate and evaporite sedimentary facies and their ancient analogues* (Vol. 43, pp. 149–182). International Association of Sedimentologists, Special Publication.

Sweeney, R. E., & Kaplan, I. R. (1973). Pyrite framboid formation: Laboratory synthesis and marine sediments. *Economic Geology, 68,* 618–634.

Taberner, C., Cendón, D. I., Pueyo, J. J., & Ayora, C. (2000). The use of environmental markers to distinguish marine vs. continental deposition and to quantify the significance of recycling in evaporite basins. *Sedimentary Geology, 137,* 213–240.

Topper, R. P. M., & Meijer, P. T. (2013). A modeling perspective on spatial and temporal variations in Messinian evaporite deposits. *Marine Geology, 336,* 44–60.

Trichet, J., Défarge, C., Tribble, J., Tribble, G., & Sansone, F. (2001). Christmas Island lagoonal lakes, models for the deposition of carbonate–evaporite–organic laminated sediments. *Sedimentary Geology, 140,* 177–189.

Tucker, M. E. (1976). Quartz replaced anhydrite nodules ('Bristol Diamonds') from the Triassic of the Bristol District. *Geological Magazine, 113,* 569–574.

Tucker, M. E. (1991). Sequence stratigraphy of carbonate–evaporite basins: Models and application to the Upper Permian (Zechstein) of northeast England and adjoining North Sea. *Journal of the Geological Society, London, 148,* 1019–1036.

Ulmer-Scholle, D. S., Scholle, P. A., & Brady, A. V. (1993). Silicification of evaporites in Permian (Guadalupian) back-reef carbonates of the Delaware Basin, west Texas and New Mexico. *Journal of Sedimentary Petrology, 63,* 955–965.

Utrilla, R., Pierre, C., Ortí, F., & Pueyo, J. J. (1992). Oxygen and sulfur isotope composition as indicators of the origin of Mesozoic and Cenozoic evaporites from Spain. *Chemical Geology, 102,* 229–244.

Wardlaw, N. C., & Schwerdtner, W. M. (1966). Halite–anhydrite seasonal layers in the Middle Devonian Prairie evaporite formation, Saskachewan, Canada. *Geological Society American Bulletin, 77,* 331–342.

Warren, J. K. (1991). Sulfate dominated sea-marginal and platform evaporative settings. In J. L. Melvin (Ed.), *Evaporites, petroleum and mineral resources: Developments in sedimentology* (Vol. 50, pp. 477–533). Amsterdam: Elsevier.

Warren, J. K. (2006). *Evaporites: Sediments, resources and hydrocarbons* (p. 1019). Berlin: Springer.

Warren, J. K. (2010). Evaporites through time: Tectonic, climatic and eustatic controls in marine and nonmarine deposits. *Earth-Science Reviews, 98,* 217–268.

Warren, J. K. (2016). *Evaporites. A geological compendium* (p. 1813). Berlin: Springer.

Warren, J. K., & Kendall, C. G. S. C. (1985). Comparison of sequences formed in marine sabkha (subaerial) and salina (subaqueous) settings; modern and ancient. *American Association Petroleum Geologists Bulletin, 69,* 1013–1023.

Ziegler, P. A. (1988). *Evolution of the Arctic–North Atlantic and the Western Tethys* (AAPG Mem. 43, p. 198). Tulsa, Oklahoma: American Association of Petroleum Geologists.

Affiliations

Adrián López-Quirós[1] · Mickael Barbier[2] · José M. Martín[3] · Xavier Guichet[2]

✉ Adrián López-Quirós
alquiros@iact.ugr-csic.es

[1] Instituto Andaluz de Ciencias de la Tierra, CSIC-Universidad de Granada, Avda. las Palmeras 4, 18100 Armilla, Granada, Spain

[2] IFP Énergies Nouvelles, 1-4 Avenue de Bois-Préau, 92852 Rueil-Malmaison, France

[3] Departamento de Estratigrafía y Paleontología, Universidad de Granada, Campus de Fuentenueva s.n., 18002 Granada, Spain